



ΕΘΝΙΚΟ ΜΕΤΣΟΒΙΟ
ΠΟΛΥΤΕΧΝΕΙΟ

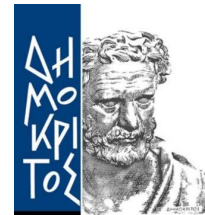
ΣΧΟΛΗ ΕΦΑΡΜΟΣΜΕΝΩΝ
ΜΑΘΗΜΑΤΙΚΩΝ
ΚΑΙ ΦΥΣΙΚΩΝ ΕΠΙΣΤΗΜΩΝ

ΣΧΟΛΗ ΜΗΧΑΝΟΛΟΓΩΝ
ΜΗΧΑΝΙΚΩΝ

ΕΚΕΦΕ "ΔΗΜΟΚΡΙΤΟΣ"

ΙΝΣΤΙΤΟΥΤΟ ΝΑΝΟΕΠΙΣΤΗΜΗΣ
ΚΑΙ ΝΑΝΟΤΕΧΝΟΛΟΓΙΑΣ

ΙΝΣΤΙΤΟΥΤΟ ΠΥΡΗΝΙΚΗΣ ΚΑΙ
ΣΩΜΑΤΙΔΙΑΚΗΣ ΦΥΣΙΚΗΣ



Διατμηματικό Πρόγραμμα Μεταπτυχιακών Σπουδών «Φυσική και Τεχνολογικές Εφαρμογές»

Προσομοίωση ανιχνευτή MicroMegas και εφαρμογή του στη ραδιογραφία ηφαιστειών με κοσμικά μίονια

ΜΕΤΑΠΤΥΧΙΑΚΗ ΔΙΠΛΩΜΑΤΙΚΗ ΕΡΓΑΣΙΑ

της

Χαρής Κιτσάκη

Επιβλέπων:

Θεόδωρος Αλεξόπουλος

Καθηγητής Ε.Μ.Π

ΑΘΗΝΑ

Φεβρουάριος 2018



ΕΘΝΙΚΟ ΜΕΤΣΟΒΙΟ ΠΟΛΥΤΕΧΝΕΙΟ
ΣΧΟΛΗ ΕΦΑΡΜΟΣΜΕΝΩΝ ΜΑΘΗΜΑΤΙΚΩΝ & ΦΥΣΙΚΩΝ ΕΠΙΣΤΗΜΩΝ
ΤΟΜΕΑΣ ΦΥΣΙΚΗΣ
ΕΡΓΑΣΤΗΡΙΟ ΠΕΙΡΑΜΑΤΙΚΗΣ ΦΥΣΙΚΗΣ ΥΨΗΛΩΝ ΕΝΕΡΓΕΙΩΝ
& ΣΥΝΑΦΟΥΣ ΟΡΓΑΝΟΛΟΓΙΑΣ

Προσομοίωση ανιχνευτή MicroMegas και εφαρμογή του στη ραδιογραφία ηφαιστείων με κοσμικά μίονια

ΜΕΤΑΠΤΥΧΙΑΚΗ ΔΙΠΛΩΜΑΤΙΚΗ ΕΡΓΑΣΙΑ

της

Χαράς Κιτσάκη

Επιβλέπων: Θεόδωρος Αλεξόπουλος
Καθηγητής Ε.Μ.Π.

Εγκρίθηκε από την τριμελή εξεταστική επιτροπή στις Φεβρουαρίου 2018.

.....
Θ. Αλεξόπουλος
Καθηγητής Ε.Μ.Π.

.....
Σ. Ματζέζος
Αν. Καθηγητής Ε.Μ.Π.

.....
Κ. Αθανασάς
Επ. Καθηγητής Ε.Μ.Π.

Αθήνα, Φεβρουαρίου 2018

.....
Χαρά Κιτσάκη
Φυσικός Εφαρμογών

© (2018) Εθνικό Μετσόβιο Πολυτεχνείο. *All rights reserved.*

Απαγορεύεται η αντιγραφή, αποθήκευση και διανομή της παρούσας εργασίας, εξ ολοκλήρου ή τμήματος αυτής για εμπορικό σκοπό. Επιτρέπεται η ανατύπωση, αποθήκευση και διανομή για σκοπό μη κερδοσκοπικό, εκπαιδευτικό ή ερευνητικής φύσεως, υπό την προϋπόθεση να αναφέρεται η πηγή προέλευσης και να διατηρείται η παρούσα σημείωση. Ζητήματα που αφορούν την εκτίμηση της εργασίας για κερδοσκοπικό σκοπό πρέπει να απευθύνονται προς τον συγγραφέα. Οι απόψεις και τα συμπεράσματα που περιέχονται σε αυτή τη δήλωση εκφράζουν τον συγγραφέα και δεν πρέπει να θεωρηθεί ότι αντιπροσωπεύουν τις επίσημες θέσεις του Εθνικού Μετσόβιου Πολυτεχνείου.

Περίληψη

Το μόνιο είναι ασταθές στοιχειώδες σωματίο και ταξινομείται μαζί με το ηλεκτρόνιο, το τ-σωματίδιο και τα αντίστοιχα νετρίνα τους στην κατηγορία των λεπτονίων. Έχει αρνητικό φορτίο, ιδιοστροφορμή 1/2 και μάζα $105.7 \text{ MeV}/c^2$ (207 φορές πιο βαρύ από το ηλεκτρόνιο). Τα μόνια παράγονται στην ατμόσφαιρα (πάνω από 15 km από την επιφάνεια της θάλασσας) και είναι αποτέλεσμα αλληλεπιδράσεων μεταξύ των πρωταρχικών κοσμικών ακτίνων και των μορίων της ατμόσφαιρας. Ο σχετικά μεγάλος χρόνος ζωής (2.2 μs), το μεγάλο εύρος ενεργειών (MeV - TeV) και η ασθενής αλληλεπίδρασή τους με την ύλη είναι μερικά από τα χαρακτηριστικά που τα καθιστούν ικανά να διασχίζουν μεγάλους όγκους ύλης.

Αξιοποιώντας το γεγονός ότι τα μόνια συνεχίζουν ανενόχλητα την πορεία τους αν δεν συναντήσουν κάποιο εμπόδιο και την απορρόφησή τους ή την εκτροπή τους όταν συναντήσουν κάποια στερεή επιφάνεια δίνεται η δυνατότητα παραγωγής εικόνας του εσωτερικού γεωλογικών δομών. Η τεχνική αξιοποίησης των μιονίων για τη σάρωση του εδάφους, γνωστή ως ραδιογραφία με μόνια, εισηγήθηκε για πρώτη φορά τη δεκαετία του 1950. Βρίσκει εφαρμογή σε πολλά πεδία, όπως η αρχαιολογία, η γεωλογία, η ασφάλεια, κ.α..

Μεταξύ των ανιχνευτών που χρησιμοποιούνται για τέτοιου είδους εφαρμογές, μία πολλά υποσχόμενη επιλογή αποτελεί η τεχνολογία των ανιχνευτών MicroMegas. Ο ανιχνευτής MicroMegas ανήκει στην κατηγορία των ανιχνευτών αερίου, έχει μικρό κόστος κατασκευής, παρουσιάζει αντοχή σε περιβάλλον υψηλής ακτινοβολίας και παρέχει πολύ καλή χωρική και ενεργειακή διακριτική ικανότητα. Τέλος, καθιστά δυνατή την παρακολούθηση σε πραγματικό χρόνο του υπό μελέτη συστήματος. Έχει χρησιμοποιηθεί ήδη σε πολλά πειράματα στο CERN και έχει επιλεγεί για την αναβάθμιση του New Small Wheel του θαλάμου μιονίων του πειράματος ATLAS.

Η παρούσα διπλωματική εργασία εκπονήθηκε στα πλαίσια της ολοκλήρωσης των μεταπτυχιακών μου σπουδών και αποτελεί μία εισαγωγή της μελέτης του εσωτερικού ηφαιστειακών δομών με τη χρήση μιονίων.

Στο Κεφάλαιο 1 γίνεται μία ιστορική αναδρομή της ανακάλυψης των κοσμικών ακτίνων.

Το δεύτερο Κεφάλαιο ασχολείται με τα κοσμικά μόνια, την παραγωγή τους, τη ροή τους στην επιφάνεια της γης, την αλληλεπίδρασή τους με την ύλη καθώς και με την περιγραφή της μεθόδου αξιοποίησή τους για την τομογραφία μεγάλων δομών.

Στο τρίτο Κεφάλαιο γίνεται μία περιγραφή της κίνησης και της αλληλεπίδρασης φορτισμένων σωματιδίων σε αέριο μέσο, η περιγραφή του ανιχνευτή MicroMegas καθώς και η προσπάθεια μελέτης του μέσω προσομοιώσεων.

Στο Κεφάλαιο 4, εξετάζεται μέσω προσομοιώσεων, το εύρος και η απώλεια ενέργειας των μιονίων καθώς διασχίζουν πέτρωμα πυκνότητας $2.6 \text{ g}/\text{cm}^3$ (μέση πυκνότητα γήινων πετρωμάτων). Στη συνέχεια κατασκευάστηκε η υπό μελέτη δομή με τη μορφή voxels διαστάσεων $25 \times 25 \text{ m}$, το κέντρο των οποίων αντιστοιχεί στις συντεταγμένες των τοπογραφικών δεδομένων που αντλήθηκαν από δορυφορικές απεικονίσεις της περιοχής. Για την παραπάνω δομή και για μόνια τα οποία διασχίζουν οριζόντια τη γη (πιο ενεργητικά σε σχέση με αυτά που τη διασχίζουν κατακόρυφα) μελετήθηκε το φαινόμενο της σκέδασης καθώς και η ενέργεια που αφήνουν στον ανιχνευτή κατά την έξοδό τους από το ηφαίστειο.

Abstract

The muon is an unstable elementary particle and is classified with the electron, the τ -particle and their neutrinos as a lepton. It has a negative electric charge, an angular momentum of $1/2$ and a mass of $105.7 \text{ MeV}/c^2$ (207 times heavier than the electron). They are generated at high altitudes (15 km above sea level) when cosmic rays collide with particles in our upper atmosphere. Their relatively high mean lifetime (2.2 μs), their wide energy spectrum (MeV - TeV) and their small interaction cross section with matter are some of the properties that make them capable to penetrate through some km of matter.

By using the fact that muons can pass without significant change of their direction of motion if they do not encounter any obstacle and their absorption or diversion when they move in a thick layer of matter, an image of the interior of geological structures can be produced. This technique is known as muon tomography and it was introduced for the first time in 1950s. It meets a wide range of applications including archeology, geology, security, etc..

Among the detectors used for these applications a promising technology is MicroMegas. It is a gaseous detector, with a low construction cost, a tolerance at high radiation environment and a very good spatial and energy resolution. To end up, it can make a real-time radiography of an unknown structure possible. This technology has been used so far in many experiments at CERN and is chosen for the New Small Wheel upgrade at the ATLAS experiment.

The present diploma thesis is an introduction of the study of volcanoes by using cosmic muons.

In the first Chapter there is a brief description of cosmic rays and their history.

Chapter 2 presents cosmic muons, their formation in the atmosphere, their flux at the Earth's surface and the physics of interaction with materials. The description of muon radiography of volcanoes is summarized.

Chapter 3 deals with the transportation of charged particles in gases, the description of the MicroMegas detector and an attempt of simulation study of its behavior in the presence of a small amount of air in the gas mixture.

Chapter 4 studies through Monte-Carlo simulations, the range and the mean energy loss of muons while passing through rock of density $2.6 \text{ g}/\text{cm}^3$ (mean density of rock). In addition, the geometry under study is constructed as a number of voxels of dimensions $25 \times 25 \text{ m}$. The center of each voxel is defined by the topographic data that were extracted by satellite imagery techniques. For the above geometry and only for horizontal muons (more energetic than vertical ones) a study for the scattering effect and for the energy distribution in the detector volume was made.

Ευχαριστίες

Με την ολοκλήρωση της παρούσας διπλωματικής εργασίας θα ήθελα να εκφράσω τις ειλικρινείς μου ευχαριστίες σε όλους όσους με βοήθησαν και με στήριξαν καθ' όλη τη διάρκειά της.

Αρχικά, θα ήθελα να ευχαριστήσω τον επιβλέποντα καθηγητή μου, κ. Θεόδωρο Αλεξόπουλο για την εμπιστοσύνη που μου έδωσε, καθώς επίσης και για την καθοδήγηση και τη βοήθεια που μου παρείχε από τις προπτυχιακές μου σπουδές μέχρι και σήμερα.

Ευχαριστώ θερμά τον Κωνσταντίνο Αθανασά, για την πρόταση του θέματος, την στήριξη, την καθοδήγηση και για όλα όσα μου έμαθε αυτό το διάστημα.

Θα ήθελα να ευχαριστήσω τον Αν. Καθηγητή, κ. Σταύρο Μαλέζο για τις συμβουλές και τις εύστοχες παρατηρήσεις του καθ' όλο αυτό το διάστημα.

Θα ήθελα επίσης να ευχαριστήσω όλη την ερευνητική ομάδα πειραματικής φυσικής υψηλών ενεργειών του Ε.Μ.Π.

Ευχαριστώ τους συμφοιτητές μου Χρήστο Παρασκευόπουλο, Φώτη Κουτρούλη, Πολυεϊκή Τζανή και Άννα Σινοπούλου για τις συζητήσεις και την υποστήριξή τους.

Τέλος ευχαριστώ τους γονείς μου και τους φίλους μου για την υποστήριξη και την αγάπη τους.

Contents

| | |
|---|-----------|
| Contents | xi |
| 1 Cosmic rays | 3 |
| 2 Muon radiography | 9 |
| 2.1 Muons | 9 |
| 2.2 Energy spectrum and angular dependence at sea level | 9 |
| 2.3 Interaction with matter | 11 |
| 2.3.1 Multiple Coulomb scattering | 11 |
| 2.3.2 Energy loss | 12 |
| 2.4 Tomography of volcanoes | 13 |
| 2.4.1 Cosmic ray muon tomography | 13 |
| 2.4.2 Timeline and Applications | 13 |
| 2.4.3 Principle | 13 |
| 2.4.4 Pros and cons | 14 |
| 2.4.5 Detectors | 14 |
| 3 Micromegas detector | 15 |
| 3.1 Transportation of electrons and ions in gases | 15 |
| 3.1.1 Ionization and excitation mechanisms | 16 |
| 3.1.2 Avalanche formation and statistics | 17 |
| 3.2 Energy loss in thin absorbers | 18 |
| 3.3 Micromegas operation principle | 18 |
| 3.4 Micromegas gas mixture | 18 |
| 3.5 Simulation of Micromegas detector | 20 |
| 3.5.1 Gmsh | 20 |
| 3.5.2 Elmer | 20 |
| 3.5.3 Garfield++ | 21 |
| 3.5.4 ROOT | 22 |
| 3.6 Geometry and electric fields | 22 |
| 3.6.1 Energy in drift region | 23 |
| 3.6.2 Electrons starting with some energy | 23 |
| 3.6.3 Presence of air in detector's volume | 24 |
| 3.7 Muon telescopes for volcano tomography | 28 |
| 4 Simulation study of volcano radiography with muons | 29 |
| 4.1 Geometry | 31 |
| 4.2 Muon source | 32 |
| 4.3 Coulomb Interactions | 32 |
| 4.3.1 Energy loss and range study | 32 |
| 4.3.2 Scattering study | 34 |
| 4.4 Energy distribution in detector | 40 |
| 5 Conclusions and future directions | 41 |
| List of Figures | 43 |

Cosmic rays

After the discovery of radioactivity by H. Becquerel and M. Curie in 1896, it was generally believed that atmospheric electricity, ionization of the air, was caused only by radiation from radioactive elements in the ground or the radioactive gases or isotopes of radon they produce. If that assumption was correct, the effect should be stronger near the earth's surface and become progressively weaker with increasing altitude. In 1912, V. Hess, initiated a series of balloon flights carrying with him three Wulf's type electroscopes. The results of his observations were unexpected. He found that the ionization became somewhat weaker at first, but above 2,000 feet it began to increase gradually with altitude. He explained his results by assuming that a radiation of very great penetrating power enters our atmosphere from above.

The work of Millikan and Regener involving measurements made under water and at high altitudes respectively, confirmed Hess's assumption. It was Millikan who gave the name of cosmic rays to this radiation. Questions about cosmic rays' origin, their energy distribution, etc soon came to the surface, so a new series of experiments was developed to give answers.

To answer these questions it should be mentioned, first, what was known about atoms and radiations by then. It was found out that atoms consist of a positively charged nucleus surrounded by a cloud of negatively charged electrons and the description of their behaviour can be explained by a new physics theory, quantum mechanics. Measurements of masses, electric charges and approximation of sizes were made but very little was known about their structure. On the other hand, it was well understood that all radiations are energy carriers and they give a part or all of their energy to an appropriate absorber. The radiations known, included beta rays, or high-speed electrons emitted in the spontaneous decay of certain radioactive atoms, alpha rays, or helium nuclei emitted in the spontaneous decay of radioactive atoms, artificially accelerated particles such as cathode rays, which are electrons emitted by cathode during the discharge in a vacuum tube, visible light, infrared and ultraviolet rays, X-rays and gamma-rays.

From the end of nineteenth century, the common practice to detect radiation was by their property of ionizing gases.

Charged particles lose their energy bit by bit through a large number of ionization events. A beam of particles, all having the same mass, charge, and initial kinetic energy, will slow down at almost exactly the same rate as they travel through matter.

However, photons can too ionize gases, but by a different process, the Compton collision, which is occurred by chance. In other words, a photon may undergo such a collision almost immediately or after traveling a considerable distance. It is mentioned that a photon loses most, or perhaps all of its energy in a single encounter. Consequently, in a beam of photons that has traveled a certain distance, some photons still have the same energy they started with, while others have lost a large fraction of their energy in Compton collisions. So, in the case of a photon beam, it can only be predicted the average behavior of the particles.

The most penetrating radiation known at that time, consisted of gamma rays from radioactive substances. Additionally, it had been found experimentally that the most energetic gamma rays were also the most penetrating. That was the reason which convinced most of the physicists that cosmic rays were simply photons of greater energy than previously discovered.

In 1920, Millikan proposed a theory that energetic gamma rays were produced in interstellar space as products of the fusion of hydrogen atoms into heavier elements, and that secondary electrons were produced in the atmosphere by Compton scattering of gamma rays.

The work of Bothe and Kohlhörster was a milestone in the history of cosmic rays. In their experiments, they had set up two Geiger-Müller (G-M) counters, each connected to an electroscope. When placed one above the other at a small distance apart, they noticed simultaneous coincidences, that they could not be entirely due to chance, because they became much less frequent when the distance between the two counters was increased. A photon could, in principle, produce a coincidence by a double Compton effect, but the probability of a Compton collision in the wall or in the gas of the counter is very small, so the probability of two Compton collisions is quite negligible. They rightly concluded, that the observed coincidences must be due to the passage of individual charged particles. That particles could not be ordinary alpha or beta rays, because counters' walls would stop all such particles. Placing a gold block of 4.1 cm thick between the counters (only particles with range greater than 4.1 cm of gold could traverse both counters and produce coincidences) they found that the rate of coincidences was still 76%

of what it had been without the block. The results had failed to provide any support for the accepted view of cosmic rays as high-energy photons and had thrown the question wide open.

In 1930, B. Rossi was curious to find out if the cosmic-ray particles found near the sea could also traverse much larger thicknesses of matter such as lead. He arranged three G-M counters along a vertical line placing between them bricks of lead which were increasing to a total of 1m. He found that 60% of the cosmic-ray particles capable of traversing 25cm of lead also traversed 1m of lead. So, cosmic-ray particles, whatever their nature, had to be many orders of magnitude more energetic than beta rays. In 1929, Skobelzyn working with a cloud chamber placed in a magnetic field, had photographed the tracks of unusually energetic negative particles passing through the chamber. In his pictures he pointed out the appearance of two and in one case of three tracks in the same picture. To investigate the suspected production of secondary particles by cosmic rays in matter, Rossi placed three G-M in a triangular array surrounded by lead. The array recorded a large number of coincidences. With the upper part of lead shielding removed, the coincidence rate fell almost to zero. The unexpected finding was the great abundance of secondary rays, which was meant that a significant fraction of particles observed near the sea level had been produced in the atmosphere.

A way to analyze cosmic rays is by using the earth as a magnet. If the primary rays are electrically charged particles, they will be deflected by the earth's field in one direction or the other depending on their charge. If they are neutral particles or photons, they will pass through the field undeflected. The magnetic field surrounding the earth resembles the one of a magnetic dipole, the field that would be produced by a bar magnet short in comparison with the radius of the earth, located near the earth's center and with its north pole toward the geographic south and its south pole toward the geographic north. Such a field is not uniform. The magnetic lines are curved and the field strength varies from point to point, decreasing with increasing distance from the center of the dipole. A moving charged particle in a magnetic field experiences a deflecting force, its direction is given by the right-hand rule. As a consequence, a positively charged particle must move clockwise with respect

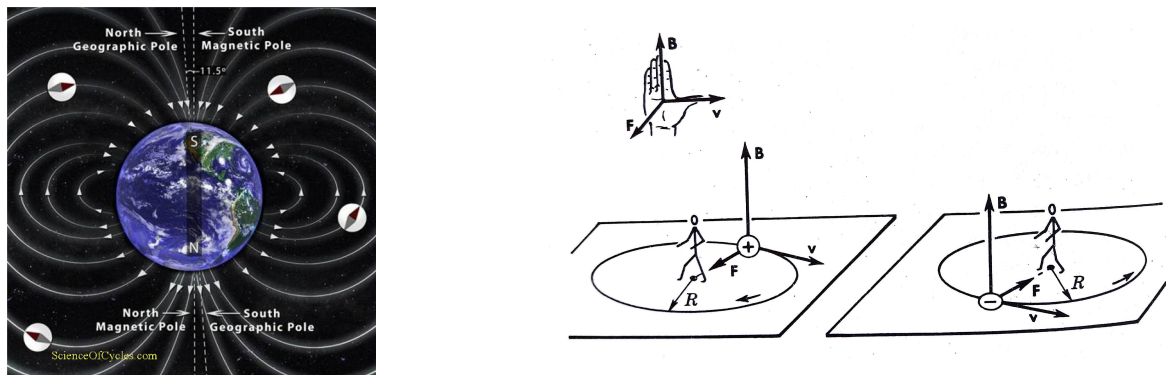


Figure 1.1: Left: Earth's magnetic field, Right: The direction of motion of a positively and a negatively charge in the presence of magnetic field[1]

to an observer lined up with the magnetic field, whereas a negatively charged particle moves counter-clockwise on the same conditions. In 1930, it was thought that if primary cosmic-ray particles were electrically charged, they would be somehow channeled toward the poles along the magnetic lines. Then, at high latitudes, the cosmic-ray intensity should be greater than in the equatorial regions. Measurements were taken at different latitudes but no significant changes were found.

In 1931, B. Rossi used cosmic-ray telescopes (two or more G-M counters in coincidence arranged with their centers on a straight line) so as to investigate the east-west effect¹ proposed by Störmer. By changing the orientation of the telescope, it then became possible to compare the numbers of cosmic-ray particles arriving from different directions. No significant differences were found but, later in 1933, as the first concrete evidence for the existence of a latitude effect was beginning to appear, the east-west effect was discovered in three separate experiments. It was found that the intensity of cosmic rays was greater from west than from the east. It was thus clear that a portion, possibly all, of the primary cosmic radiation consisted of positively charged particles.

One year after, in 1932, a new positively charged particle, the positron, had been discovered by Carl D. Anderson and its strange ability of its birth and disappearance was of great importance.

In 1934, Hans A. Bethe and W. Heitler had considered in detail what happens when a charged particle passes near an atomic nucleus and its trajectory is bent by the strong electric field associated with the positive electric charge of the nucleus. According to the classical theory of electric and magnetic fields, any accelerated charge emits electromagnetic waves. Since the motion along a curved trajectory is an accelerated motion, charged particles passing near a nucleus must radiate, in other words they must emit photons. That theory gave the key to the explanation of cosmic-ray showers: A high energy photon enters in matter. After traveling a short distance it disappears, giving rise to an electron-positron pair which between them share the energy of the incident photon. The two electrons, do not travel far before each of them radiates a photon, losing a large fraction

¹Positively charged primary cosmic rays should arrive in smaller numbers from the eastern than from the western regions of the sky. If primary cosmic rays are negatively charged the situation is reversed. The east-west effect can reveal the sign of primary cosmic ray charge.

of its energy. The newly created photons soon materialize again and the process continues. As a result, the particles increase in number while their energy decreases. The successful interpretation of showers proved that a part of cosmic ray particles found in the atmosphere includes high energy electrons and photons. However, the existence of the penetrating particles could

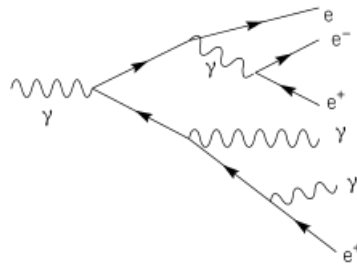


Figure 1.2: Development of a shower in matter through successive events of pair-production and radiation [1]

not be explained by that theory and their nature remained a puzzle.

Street and Stevenson used a cloud chamber, in a magnetic field, which was triggered with an arrangement of G-M counters that signaled when a particle entering the chamber failed to come out of its walls. Their philosophy was to produce useful pictures of low-energy penetrating particles and they finally achieved to determine in 1937, the existence of a new particle of a mass of approximately 200 electron masses. This new particle named meson (when investigations revealed the existence of other mesons physicists called that first-discovered meson as muon). The nature of the local cosmic radiation observed in the atmosphere was now clear. Mesons (penetrating particles), electrons (absorbed particles) and photons (non-ionizing particles) were all of the radiation found near sea level.

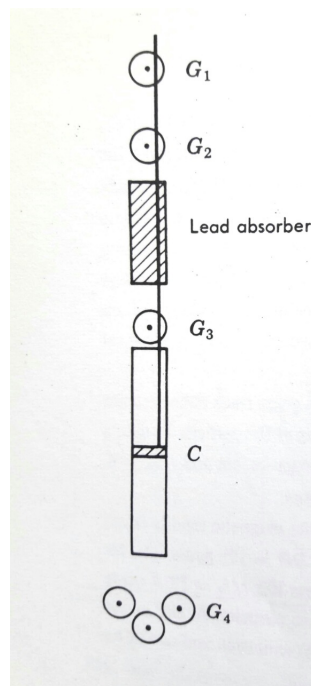


Figure 1.3: Experimental arrangement used by Street and Stevenson to obtain pictures of low-energy penetrating particles [1]

Between 1936 and 1937 several measurements of the numbers of cosmic ray particles found at different altitudes in the atmosphere, were developed. It was found that (a) air absorbed cosmic rays more effectively than solid or liquid matter did of the same mass per unit area and (b) the thinner air at very high altitudes appeared to be a better absorber than the denser air in the lower atmosphere. In 1938 H. Kuhlenskampff pointed out that if the penetrating particles could decay spontaneously, an explanation for the anomalous absorption of cosmic ray particles in air could be given. The first cloud chamber picture of such a decay was obtained by Williams and G. E. Roberts in England. A positively charged particle had stopped in the gas of the chamber and at the end of its track had appeared the track of a positron.

The cloud chamber is a really wonderful device but it has inherent limitations. Because of the low density of gases, very few of the particles entering its walls, eventually collide with gas nuclei or stop within it. To overcome that issue, physicists in the 1930s began to build larger chambers and to place slabs of solid materials across them. Later, in the middle 1940s they succeeded in perfecting a detector with the desired properties, the so-called nuclear emulsion.

In 1947 C.M.G. Lattes, Occhialini and Powell exposed some nuclear emulsions to cosmic rays at mountain altitudes. In these plates, they found several pictures that depicted three tracks of three different particles. The first particle that enters the plate appears to have a mass several hundred times than of an electron. The second one, which comes to rest in emulsion after traveling a distance of slightly more than 0.5mm, also appears to have a mass of a few hundred electron masses but lighter than the first. The third one is recognised as an electron. The conclusion derived is that the pictures showed the decay of one meson into a lighter one. The heavier became known as the pion meson while the lighter one was recognised as the first discovered meson and named after muon.

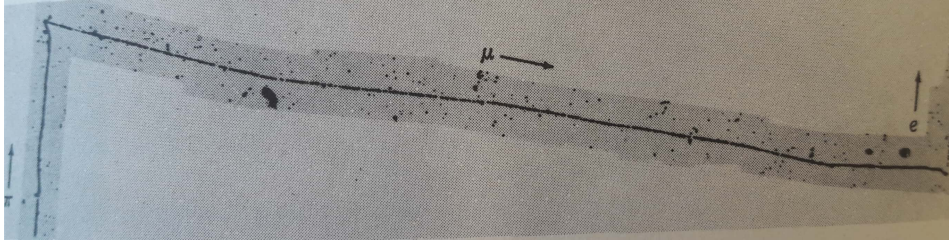


Figure 1.4: Photomicrograph of tracks in a nuclear emulsion [1]

Every particle has a corresponding antiparticle of opposite charge but of equal mass. Before the discovery of pion, physicists believed and proved through experiments that positive and negative mesons (muons) should behave in a characteristically different manner after coming to rest in matter. A positive meson, can never approach very close to an atomic nucleus because of the repulsion exerted by the positive nuclear charge. Therefore, it will wait around until it disappears by a spontaneous decay. A negative one, will be predominately absorbed by the absorber's nuclei depending on the interaction's strength. Another fact that was observed was that nuclear capture became increasingly effective with increasing absorber's atomic number. However, it was extremely difficult to explain how negative mesons could possibly escape nuclear capture. The proof that muons are products of pions and not the particles produced in high-energy nuclear interactions made the image clear. Muon mesons do not interact strongly with nuclei. If pions were abundantly produced in nuclear interactions, then negative pions that stopped in matter were also captured promptly by nuclei. But, there was not seen any picture of negative pion decaying into muon but a star is produced by the particles into which the nucleus disintegrates as a result of an explosion.

Only charged mesons had been discovered so far. Soon, physicists started to think of the existence of neutral mesons. Oppenheimer in 1947, suggested that neutral mesons might decay very rapidly into photons and these photons might be responsible for most of the cosmic-ray photons and electrons found in the atmosphere. That assumption proved to be correct in 1950 with the discovery of the neutral pion.

All the experiments on the nuclear interactions of cosmic rays greatly straightened the belief that the number of nuclear-active particles, which constituted a small fraction of the total radiation found near sea level, increased with increasing altitude much more rapidly than the number of electrons, photons and muons did. Through careful analysis and discussion of the experimental data, physicists became convinced that practically all primary cosmic rays were nuclear-active particles. These particles that were found in the atmosphere were protons, neutrons and pions. The only stable positively charged particle among these was the proton. It was thus natural to conclude that primary cosmic rays were protons.

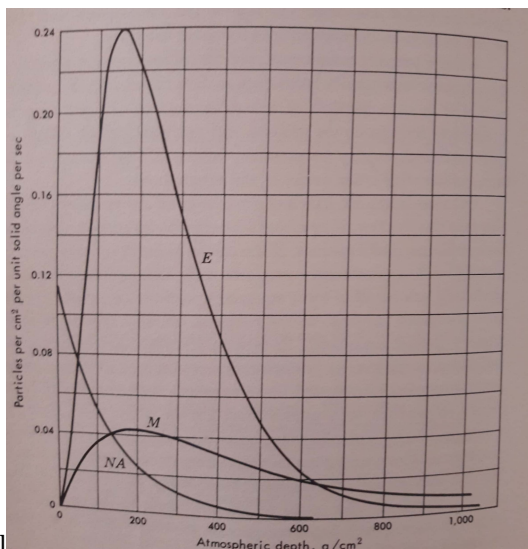


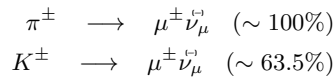
Figure 1.5: Vertical intensity of three components of local cosmic radiation as a function of atmospheric depth in grams per square centimeter. Curve NA: nuclear-active particles with energies greater than about 1BeV. Curve E: electrons with energies greater than about 100 MeV. Curve M: muons with energies greater than about 200 MeV.

atomic nuclei. By the time the shower has traveled some distance through the atmosphere, its particles are distributed over a wide area. Their density is greatest at the center (the point where the primary particle would have hit if there had been no collisions) and it decreases gradually with increasing distance from this point.

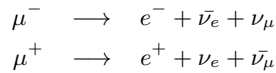
Muon radiography

2.1 Muons

As mentioned in the preceding chapter among the secondary particles arising from the collisions of primary cosmic ray particles with atomic nuclei in the atmosphere are muons. They can be produced (at very high energies, in the TeV range) by the decay of short-lived mesons ($\rho, \omega, \phi, D, J/\psi$), but their main source is from the decay of long-lived charged pions and kaons. The most important decay channels and respective branching ratios are [5]



The muon is an elementary particle similar to the electron with an electric charge of $q = -1$, an angular momentum $J = 1/2$ and a mass of $m = 105.7 MeV/c^2$ which is about 207 times heavier than the electron. In elementary particle physics the muon is classified as a lepton, as it is not believed to be composed of any simpler particles. In addition, it is unstable with a mean lifetime of $2.2\mu s^1$ and decays via the weak interaction as follows,



Muons are the most abundant charged particles arriving at sea level. They are thought to be generated at high altitudes of the atmosphere at about 15 km above sea level and travel with the other products of primary cosmic rays to the Earth in conical showers staying within about 1° of the trajectory of the primary particle which creates them. At sea level, their rate can be estimated as one muon per square centimetre, per minute and their average energy is about 4 GeV. Considering that their energy loss is about 2 MeV per g/cm^2 and that the (vertical) atmospheric depth² is about 1000 g/cm^2 , muons lose about 2 GeV in passing through the whole atmosphere. The small energy loss in the whole atmosphere, the relatively long lifetime and the fairly small interaction cross section make muons capable to penetrate deeply underground.

Muons with the highest energy that have been recorded with magnetic spectrometers have been detected in near horizontal direction which is more favorable. The reason is that very high energy pions emerging from the first generation of interactions of primaries that enter the earth's atmosphere tangentially travel longer in a low density medium than when propagating vertically. [3]

2.2 Energy spectrum and angular dependence at sea level

All long-lived unstable particles compete between interaction and decay as they propagate in the atmosphere. The probability for either process to occur depends on the lifetime of the particle, which is a function of its kinetic energy, and on the local atmospheric density, which is a function of altitude.

Below the few GeV, the muon decay probability cannot be neglected. A muon of 1 GeV has a Lorentz factor $\gamma = E_\mu/m_\mu c^2 \sim 10$ and a decay length $d_\mu = \gamma\tau_\mu c \sim 6$ km. Pions decay relatively fast (for $\gamma = 10, d_\pi \sim 78$ m), the daughter muons fail to reach

¹ because of the relativistic time dilation and the fact that they do not interact strongly with the atmospheric nuclei, most of the muons survive in the propagation in atmosphere and reach the ground

² Atmospheric depth X is defined as the integral in altitude of the atmospheric density above the observation level h ,

$$X = \int_h^\infty \rho(h') dh'$$

That formula is valid only for muons arriving vertically. For zenith angles $< 60^\circ$ (the Earth surface can be approximated as flat) the atmospheric depth is scaled with $1/\cos\theta$, giving the slant depth. For larger zenith angles, the curvature of the Earth has to be accounted for.

the sea level and they rather decay themselves or get absorbed in the atmosphere. To the limit of $E_\mu \leq 1 \text{ GeV}$, muon decay and energy loss are important and the energy spectrum is almost flat.

At higher energies, the situation changes. For pions of 100 GeV ($d_\pi \sim 5.6 \text{ km}$, corresponding to a column density of 160 g/cm^2) the interaction probability starts to dominate over decay. Pions of these energies will produce further pions, which will also decay eventually into muons (of lower energy). Therefore, the muon spectrum at high energies is always steeper compared to the parent pion spectrum.

For $1 \text{ GeV} \leq E_\mu \leq \epsilon_{\pi,K}$ ($\epsilon_\pi = 115 \text{ GeV}$, $\epsilon_K = 850 \text{ GeV}$, the critical energies for the vertical directions) almost all mesons decay and the muon flux has the same power law of the parent mesons and is independent on the zenith angle.

For $E_\mu \gg \epsilon_{\pi,K}$, the meson production spectrum has the same power law of the primary cosmic rays, but the rate of their decay steepen one power of E_μ , since the pion and kaon decay probability is suppressed (the thickness of the atmosphere is not large enough for pions to decay due to high Lorentz factor). The muon spectrum is flatter than the vertical one and its flux is respectively higher.

In the intermediate and high energy region (above 100 GeV) and for zenith angles $\theta < 60^\circ$ the below formula stands:

$$\frac{dN_\mu}{dE_\mu} \approx \frac{0.14E^{-2.7}}{\text{cm}^2 \cdot \text{s} \cdot \text{sr} \cdot \text{GeV}} \left[\frac{1}{1 + \frac{1.1E_\mu \cos \theta}{115 \text{ GeV}}} + \frac{0.054}{1 + \frac{1.1E_\mu \cos \theta}{850 \text{ GeV}}} \right] \quad (2.1)$$

Pions decay more easily in non-vertical showers, so a zenith angle θ factor enters in the above formula and muons at large angles have a flatter energy spectrum.

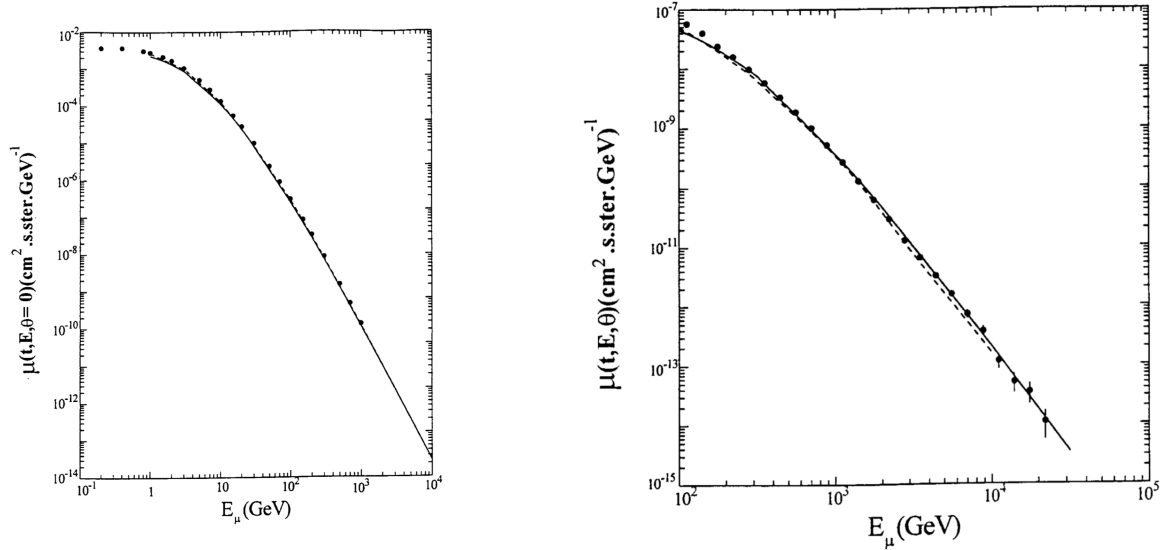


Figure 2.1: Left: Vertical muon flux at sea level. Solid line: calculated by Lipari (Lipari, 1993). Dashed line: calculated by [4]. Data: Allkofer et al., 1971.

Right: Zenithal ($\theta = 89^\circ$) muon flux at sea level. Solid line: calculated by Lipari (Lipari, 1993). Dashed line: calculated by [4]. Data: Matsumo, 1984.

At almost horizontal directions, particles have to travel bigger distances in the atmosphere than at vertical directions. As a consequence, the muon intensity at non vertical directions and at low energies is reduced because of decay and absorption. The overall angular distribution of muons measured at sea level ($E_\mu \sim 4 \text{ GeV}$) is analogous to $\cos^2 \theta$. In general, the zenith angle dependence can be expressed as

$$I(\theta, X_h, E) = I(0^\circ) \cos^{n(E, X_h)}(\theta) \quad (2.2)$$

where $I(0^\circ)$ is the vertical intensity.

2.3 Interaction with matter

2.3.1 Multiple Coulomb scattering

Moving in a medium, a charged particle changes its direction of motion as a result of interaction with the electric fields of atomic nuclei. The direction of motion changes in most cases by only a very small angle. However, because the frequency

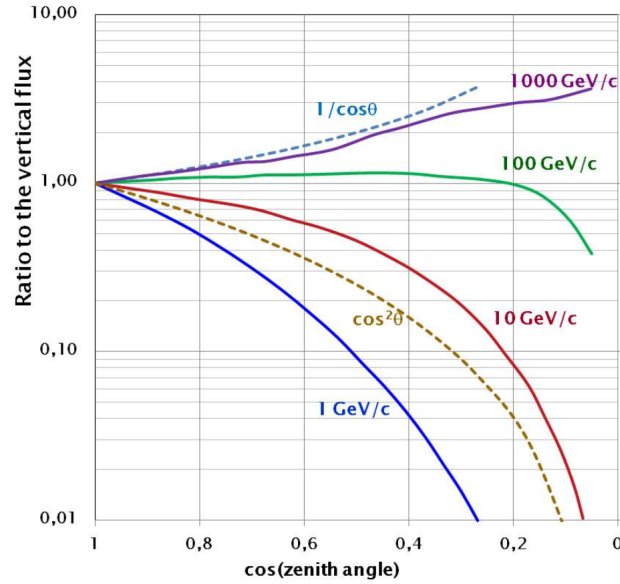


Figure 2.2: Angular distribution of muons at sea level for different muon energies [5].

of these collisions is high (on average they are occurred every $(\frac{v}{c})^2 \cdot 10^{-5} \cdot \rho^{-1} \text{ cm}$), the particle changes the direction of its motion markedly after passing through a thick layer of matter. Naming θ , the solid angle into which is concentrated the 98%

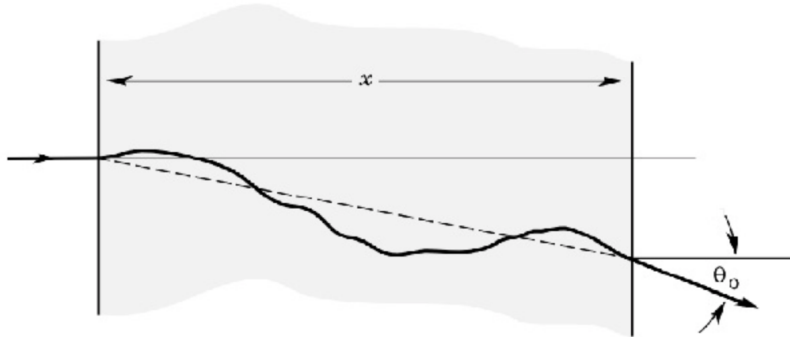


Figure 2.3: Multiple Coulomb scattering (from: meroli.web.cern.ch)

of the beam after a thickness x of the material, and if we define $\theta_0 = \frac{\theta}{\sqrt{2}}$ the projection of θ on a plane, the angular dispersion can be calculated as follows³:

$$\theta_0 = \frac{13.6}{\beta c p} z \sqrt{x/X_0} [1 + 0.038 \ln(x/X_0)] \quad (2.3)$$

where $p, \beta c, z$ are the momentum, velocity and charge number of the incident particle and x/X_0 is the thickness of the scattering medium in radiation lengths⁴.

³This formula describes scattering from a single material.

⁴Radiation length is a characteristic of the material. The radiation length for a given material consisting of a single type of nuclei can be defined by the approximated formula:

$$X_0 = \frac{716.4 \cdot A}{Z(Z+1) \ln(287/\sqrt{Z})} g \cdot \text{cm}^{-2} \quad (2.4)$$

where Z, A are the atomic and mass number of the nucleus.

2.3.2 Energy loss

Muons lose energy by ionization and excitation of atoms of the material and by radiative processes (bremsstrahlung, direct production of e^+e^- pairs, photonuclear interactions) in the field of the nucleus and of the atomic electrons [6]. The total mean energy loss per unit length of a muon traversing a material can be represented as:

$$\left(-\frac{dE}{dx}\right)_{total} = \alpha_{ion}(E) + E \cdot \left(\alpha_{pairprod}(E) + \alpha_{brems}(E) + \alpha_{photonucl}(E)\right) \quad (2.5)$$

$$\left(-\frac{dE}{dx}\right)_{total} = \left(-\frac{dE}{dx}\right)_{ioni} + \left(-\frac{dE}{dx}\right)_{brems} + \left(-\frac{dE}{dx}\right)_{pairprod} + \left(-\frac{dE}{dx}\right)_{photonuclear}$$

The mean energy loss from ionization is given by the Bethe-Bloch equation:

$$\left(-\frac{dE}{dx}\right)_{ioni} = Kz^2 \frac{Z}{A} \frac{1}{\beta^2} \left(\frac{1}{2} \ln \frac{2m_e c^2 \beta^2 \gamma^2 T_{max}}{I^2} - \beta^2 - \frac{\delta}{2} - \frac{C}{Z} \right) \quad (2.6)$$

where K is a constant, z the charge of the incident particle, $\beta = p/E$, $\gamma = E/m$, $T_{max} = \frac{2m_e c^2 \beta^2 \gamma^2}{1 + 2\gamma \frac{m_e}{m} + \left(\frac{m_e}{m}\right)^2}$ the maximum kinetic energy which can be transferred to the electrons of the medium, I the mean excitation energy of the medium, δ the density correction⁵, and C/Z the shell correction⁶.

The mean energy loss from bremsstrahlung is given by the Bethe-Heitler equation:

$$\left(-\frac{dE}{dx}\right)_{brems} = \frac{E}{X_0} \left(\frac{m_e}{m}\right)^2 \quad (2.7)$$

The mean energy loss due to pair production and photonuclear interaction with the medium is parametrized in two energy ranges:

- For $8GeV < E < 1TeV$:

$$\left(-\frac{dE}{dx}\right)_{pp+nucl} = -0.5345 \frac{1}{X_0} + 6.803 \cdot 10^{-5} \frac{E}{X_0} + 2.278 \cdot 10^{-11} \frac{E^2}{X_0} - 9.899 \cdot 10^{-18} \frac{E^3}{X_0} \quad (2.8)$$

- For $E > 1TeV$:

$$\left(-\frac{dE}{dx}\right)_{pp+nucl} = -2.986 \frac{1}{X_0} + 9.253 \cdot 10^{-5} \frac{E}{X_0} \quad (2.9)$$

E is the energy of the traversing particle in MeV.

CSDA range

Continuous slowing down approximation (CSDA) range is a very close approximation to the average path length traveled by a charged particle as it slows down to rest. In this approximation the rate of energy loss at every point along the track is assumed to be equal to the same as the total stopping power. Energy loss fluctuations are neglected. By integrating the reciprocal of the total stopping power with respect to energy we obtain the CSDA range:

$$R = \int_0^{E_0} \frac{dE}{\left(-\frac{dE}{dx}\right)_{total}} \quad (2.10)$$

where E_0 is the energy of the muon at ground level.

⁵This correction term becomes important at high energies because media have a tendency to become polarized (the medium cannot be considered as isolated) as the incident particle velocity increases.

Let $x = \log_{10}(\gamma\beta) = \ln(\gamma^2\beta^2)/4.606$ then δ is defined by

$$\begin{aligned} \delta(x) &= 0 && \text{for } x < x_0 \\ \delta(x) &= 4.606x - C + \alpha(x_1 - x)^m && \text{for } x \in [x_0, x_1] \\ \delta(x) &= 4.606x - C && \text{for } x > x_1 \end{aligned}$$

where $C = 1 + 2 \ln(I/h\nu_p)$, $h\nu_p$ the plasma energy of the medium, $\alpha = 4.606(x_\alpha - x_0)/(x_1 - x_0)^m$, $x_\alpha = C/4.606$ and $m = 3$. For condensed media:

- $I < 100eV$: $C \leq 3.681$ $x_0 = 0.2$ $x_1 = 2$
- $I < 100eV$: $C > 3.681$ $x_0 = 0.326C - 1.0$ $x_1 = 2$
- $I \geq 100eV$: $C \leq 5.215$ $x_0 = 0.2$ $x_1 = 3$
- $I \geq 100eV$: $C > 5.215$ $x_0 = 0.326C - 1.5$ $x_1 = 3$

⁶At low energies for light elements and at all energies for heavy elements the probability of collision with the electrons of the inner atomic shells (K, L, etc.) is negligible.

2.4 Tomography of volcanoes

To investigate the underground structure of a volcano, different techniques are utilized, that are sensitive to different physical properties [7]:

- Seismic approaches are based on the inversion of earthquake traveltimes data to derive a 3D image of the velocity structure. An increasingly used imaging technique, seismic interferometry, utilizes the cross-correlation of signal pairs to reconstruct the impulse response of the medium.
- Electrical resistivity tomography is sensitive to electric conductivity anomalies associated with fluid-saturated rocks and is widely used to image fluid presence.
- Gravity measurements allow the computation of Bouguer anomalies, which are reflective of anomalies in the underground density structure.

However, because of the highly heterogeneous character of the structures to be investigated, volcano imaging remains challenging. Dense measurements in active zones, imply a high level of risk for the personnel. Despite of that, strong medium heterogeneities produce notable scattering/attenuation of seismic wave and may result in high resistivity/density contrasts, which occur a non-linear inversion of the data. Finally, all these techniques do not offer the spatial resolution needed to properly characterize the interior of a volcano. To overcome these difficulties, it is advisable to find out new imaging techniques. A newly developing technique, volcano imaging through muons, has already shown great promises and the information obtained really helps to model the internal structure of volcanoes.

2.4.1 Cosmic ray muon tomography

X-rays allow us to produce pictures of the upper few cm of matter. Their ability to pass through soft parts of the human body and been absorbed in the denser bones enable us to reveal the internal attributes of the target by producing shadow pictures. By following the same principles as in X-ray tomography, we can explore the inside of large structures (eg. volcanoes, mountains, mines etc) by using cosmic ray muons, taking the advantage of their great penetration in matter. Muon radiography constitutes a ground-breaking method in assessing the density variations within rocks, and so far it has mainly been used to monitor the density variations of volcanoes and to evaluate the magma kinetics therein [25].

2.4.2 Timeline and Applications

This technique was used for the first time in 1955 to measure the depth of the overburden of a tunnel, using a Geiger counter telescope, by E. P. George [8]. Later, in 1970 L.W. Alvarez et al. carried out the same method of imaging for the search of possible hidden chambers in the Pyramid of Chephren in Egypt [9]. In 1979, the first theoretical studies of in-situ rock density determinations using cosmic ray muon intensity measurements with application in mining geophysics were developed by L. Malmqvist et al. [10].

Recently, in 1995 the first proposal of studying the inner structure of volcanoes with the use of the horizontal cosmic ray muons was made by Nagamine et al. [11]. Several projects all around the world started to use with a great success the method for the radiography of volcanoes. The first experiments have been initiated in Japan and the technique proved effective in imaging the internal structure of Mt Asama (completed in 2007) [12]. Some of the volcanoes that the method has been applied to, are Mt Usu (Japan) [13], Satsuma-Iwojima (Japan) [14], Vesuvius (Italy) [15], Etna (Italy) [16], Stromboli (Italy) [17], La Soufrière of Guadeloupe [18] and Puy de Dôme [19] (France).

Another application of the method is the imaging of nuclear reactors [20] and cargos [21].

2.4.3 Principle

A detector is placed on a slope of the volcano and is used to obtain a 2-D image of the interior. By using more detectors at different sides of the dome, 3-D images can be produced.

Muons, are capable to travel long distances in rock and their energy loss depend on the amount of matter crossed. There is a unique relationship between mean range and the intensity of muons. Once mean range is known, the minimum energy of muons that can penetrate can be determined, so the integrated flux [16]

$$I = \int_{E_{min}}^{\infty} \Phi_0 dE_0 \quad [cm^{-2} sr^{-1} s^{-1}] \quad (2.11)$$

is uniquely given. Inversely, for a specimen with an unknown range, a measurement of the muon flux penetrating through the substance with a zenith angle, uniquely determines its thickness.

The differential flux, Φ_0 , of incident cosmic muons is determined by Monte Carlo simulation codes (Heck et al., 1998) or by analytical modelling of experimental results (Gaisser, 1990). Almost all types of rocks share the same Z/A ratio and the only varying quantity is the density. Provided that the product between length of crossed rock and density remains the same, the formulation derived for the standard rock can be utilized to calculate E_{min} relative to other rock types.

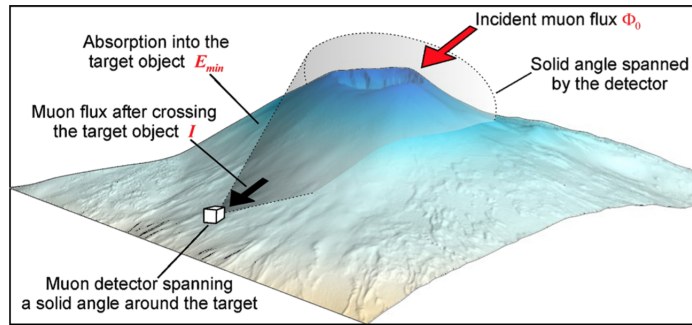


Figure 2.4: Sketch of the muon radiography principle[16]

Imaging is made through the comparison between the observed integrated muon flux and the corresponding theoretical flux (calculated under the assumption of an homogeneous target object using the theoretical incident muon flux in open sky conditions and the relevant topographic information). Once the differences between observed and theoretical integrated fluxes are estimated, by knowing the energy loss of muons through matter one can derive anomalies in the amount of matter encountered along each direction by the travelling particles. Furthermore, if the path lengths are known from topographic information, it is possible to retrieve anomalies with respect to the average density of the rock along each travelling direction.

2.4.4 Pros and cons

The method presents some advantages compared to the established geophysical techniques mentioned before. First of all, it is not necessary to use cost demanding sources as muons are naturally produced with a broad energy spectrum. Furthermore, the method has not any inherent ambiguity, so the calculation and the transition from the one property to the other is relatively simple and precise. Another advantage consists in the fact that dense measurements at not easily accessible areas are not required, so the risk of injuries is lower. Finally, the spatial resolution can reach as fine as tens of meters while other conventional methods can provide some hundreds of meters.

On the other hand, the method has some disadvantages. Due to geometrical constraints, the method can be applied only above the horizon of the detector and to have a sufficient flux, the thickness of the rock to be crossed by muons should not exceed a few kilometres. The data-taking speed is too slow (weeks, months) to detect a rapid volcanic process at the top region of the volcano.

There are cases, that the detector system is placed at a long distance from the target. The method has to confront some difficulties. Among them are the increase of background events which have to be removed as well as the contribution of a loss due to the existence of air between the target and the detector.

2.4.5 Detectors

Three types of muon detectors have been used:

- nuclear emulsion. When a charged particle passes through the nuclear emulsion all the trajectories will be recorded and can be read when the emulsion is later developed. The major advantage of nuclear emulsion detectors is their ability to operate without any electricity power. However, there is not any record of timing information.
- scintillators. The events are recorded as a flash of light generated by the incident charged particles and subsequently detected by photon-multiplier tubes. Particle trajectories can be tracked by connecting two or more vertex points determined by the geometrical address of the scintillator bars and their corresponding timings. Furthermore, scintillators can be used as real-time readers.
- gaseous detectors. This kind of detectors are utilized as real-time detectors. Although the detector requires a constant gas flow over the entire period of the measurement, it can produce high-definition volcano images. Gaseous detectors excel in spatial resolution than scintillators and they seem to be an alternative to the scintillator-based detectors , reaching the simplicity and reliability of the latter and at the same time drastically reducing the cost and weight.

Micromegas detector

Among the gaseous detectors, a promising technology for a real-time radiography of volcanoes is MicroMegas (Micro Mesh Gaseous Structure). The research of the MicroMegas detector initiated in 1990s by I. Giomataris and G. Charpak. Its development was based on the needs of nuclear and particle physics. Thanks to its high granularity it offers high spatial resolution [27]. This technology is used in several experiments in CERN including the ATLAS experiment.

3.1 Transportation of electrons and ions in gases

The motion of a charged particle in the presence of electric, \mathbf{E} , and magnetic, \mathbf{B} , fields can be expressed by P. Langevin equation:

$$m \frac{d\mathbf{u}}{dt} = e\mathbf{E} + e[\mathbf{u} \times \mathbf{B}] - \frac{m}{\tau} \mathbf{u} \quad (3.1)$$

where $-\frac{m}{\tau} \mathbf{u}$ is the force due to friction caused by the collisions of the particle of charge e , with the gas molecules, and τ is the average time between these collisions. Solving the above equation for a charged particle with a constant velocity moving within a constant electric field, its drift velocity can be determined as follows:

$$\mathbf{u} = \frac{\frac{e}{m}\tau}{1 + \omega^2\tau^2} \left(\mathbf{E} + \frac{\mathbf{E} \times \mathbf{B}}{B} \omega\tau + \frac{(\mathbf{E} \cdot \mathbf{B})\mathbf{B}}{B^2} \omega^2\tau^2 \right) \quad (3.2)$$

where $\omega = \frac{e}{m}B$ is the cyclotron frequency.

In the absence of magnetic field, $\omega\tau = 0$, \mathbf{u} is along \mathbf{E} and it can be simply expressed like:

$$\mathbf{u} = \frac{e}{m} \tau \mathbf{E} = \mu \mathbf{E} \quad (3.3)$$

where μ is the mobility of the charged particle.

On the microscopic scale, the charged particles that drift through the gas are scattered by the gas molecules so their direction of motion is randomized after each collision. For the case of an electron, because of its light mass, it scatters isotropically and it has forgotten any preferential direction. In addition to its instantaneous and randomly oriented velocity c , the electron has picked up extra velocity u , its drift velocity. There is a balance between the energy gained and the energy lost in collisions. In the next encounter, the extra energy, on the average, is lost in the collision through recoil or excitation. The total energy of an electron in the presence of an electric field constitutes of two parts, the energy received from the electric field and the energy of its thermal motion. The latter can be neglected. So, the two velocities can be approximately expressed as:

$$\begin{aligned} u^2 &= \frac{eE}{mN\sigma(\epsilon)} \sqrt{\frac{\lambda(\epsilon)}{2}} \\ c^2 &= \frac{eE}{mN\sigma(\epsilon)} \sqrt{\frac{2}{\lambda(\epsilon)}} \end{aligned} \quad (3.4)$$

where $\sigma(\epsilon), \lambda(\epsilon)$ are the electron elastic cross section and the average fractional energy loss per collision (ϵ stands for the electron's energy).

On the other hand, ions have a very different behaviour. Due to their larger mass compared to electrons, they drift much slower than the electrons, losing significant fraction of the energy acquired by each collision. As a consequence, their momentum is not randomized as much. For low values of the electric field (the ion random velocity is thermal), the drift velocity of ions is proportional to the electric field and is estimated as:

$$u = \left(\frac{1}{m} + \frac{1}{M} \right)^{1/2} \left(\frac{1}{3kT} \right)^{1/2} \frac{eE}{N\sigma} = \mu E \quad (3.5)$$

For large values of the electric field the thermal motion of the ions can be neglected and the drift velocity is proportional to \sqrt{E} :

$$u = \left(\frac{eE}{mN\sigma} \right)^{1/2} \left(\frac{m}{M} \left[1 + \frac{m}{M} \right] \right)^{1/2} \quad (3.6)$$

Electrons and ions as they drift within the gas, they experience several scatterings by the gas molecules so their drift velocity deviates from the average owing to the random nature of the collisions. These deviations correspond to a Gaussian distribution:

$$n = \left(\frac{1}{\sqrt{4\pi Dt}} \right)^3 \exp\left(\frac{-r^2}{4Dt} \right) \quad (3.7)$$

where D is the diffusion constant and with a standard deviation $\sigma_x = \sqrt{2Dt}$ (2D motion) or $\sigma_x = \sqrt{6Dt}$ (3D motion). When the energy due to the thermal motion is $\epsilon = \frac{3}{2}kT$, diffusion constant can be related to the mobility by the Einstein equation:

$$\frac{D}{\mu} = \frac{kT}{e} \quad (3.8)$$

The standard deviation as well as the diffusion constant are:

$$\sigma_x^2 = 2Dt = \frac{2DL}{\mu E} = \frac{4\epsilon L}{3eE} \rightarrow \sigma_x = \left(\frac{2kTL}{eE} \right)^{1/2}, \quad D = \frac{\mu kT}{e}$$

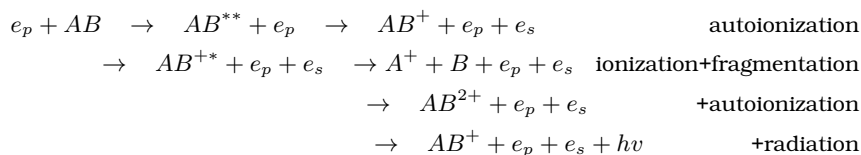
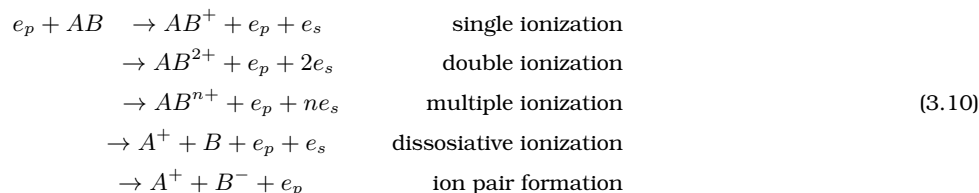
where L is the distance travelled by the particle after its starting point.

However, at high values of the electric field, the diffusion of drifting electrons in gases is not uniform in all directions, as the thermal motion is neglected. The diffusion has two components, the one along the drift direction (longitudinal diffusion) and the other perpendicular to the drift direction (transverse diffusion).

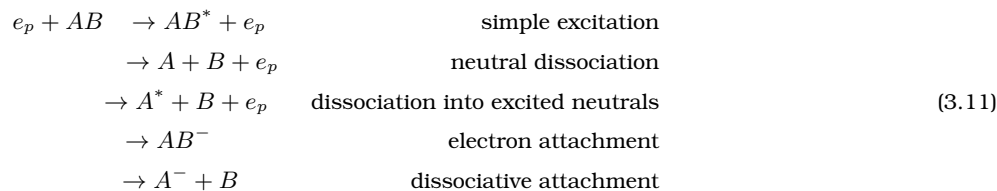
$$\sigma_l = D_l \sqrt{L}, \quad \sigma_t = D_t \sqrt{L} \quad (3.9)$$

3.1.1 Ionization and excitation mechanisms

Electrons accelerated through an electric field can collide with gas molecules either elastically or inelastically. If the electron's energy is greater than a critical value, some molecules will be ionized (noted as A^+). As the energy of the electron is increased, the ionization process will be more significant. Moreover, some of the ionized molecules may dissociate if the electron energy is sufficiently great. The interaction of a primary electron e_p with a diatomic molecule AB can precede via many channels



There are also nonionization channels



where e_s stands for the secondary, or ionized, electron.

Noble gases can form only stable negative ions at collision energies of several eV (which is higher than the energies reached during the drift in gas chambers). However, other gas molecules, are capable of attaching electrons at much lower collision energies (eg. binding energy of an electron to an oxygen atom is $\sim 0.5eV$).

A positive ion can interact with a free electron or with one of the extra electrons of a negative ion and be neutralized. In order to eliminate that effect, high electric fields help with a fast separation/collection of the charges.

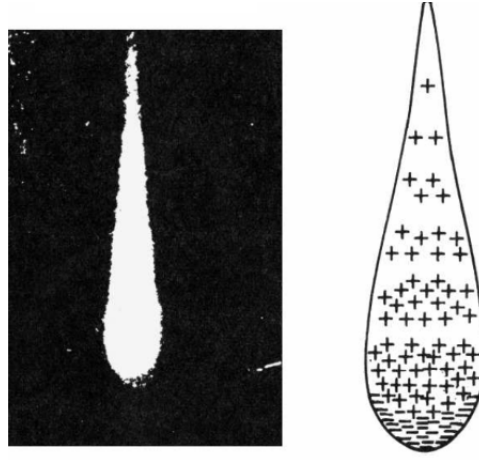


Figure 3.1: Left: Avalanche creation in a cloud chamber [33]. Right: Schematic view of the drop-like shape of an avalanche formation.

3.1.2 Avalanche formation and statistics

In the presence of high values of the electric field, electrons gain sufficient energy between two collisions such that they can ionize the medium they propagate. Electrons produced by this process may further ionize the medium. These successive ionizations form a drop-like cascade which is known as the Townsend avalanche (Townsend, 1915). Due to their high drift velocity compared to ions, electrons distribute on the head of the drop, leaving the ions on its tail.

The number of secondary ion pairs produced per unit length is described by a multiplication factor which is called the first Townsend coefficient, $\alpha = 1/\lambda$, where λ stands for the mean free path of the ionisation electron. After a path of distance dx , an initial population of electrons n_e will create dn_e electrons:

$$dn_e = n_e \alpha dx \quad (3.12)$$

For the case of a uniform electric field (α independent of the distance) by solving the above equation, the total number of electron-ion pairs produced is expressed as:

$$n = n_0 e^{\alpha x}$$

where the ratio n/n_0 is the multiplication factor called gas gain, G . For non-uniform electric fields the factor G is derived from:

$$G = \exp\left(\int_{x_1}^{x_2} \alpha(x) dx\right) \quad (3.13)$$

However, the interactions between electrons and gas atoms are dominated by statistical fluctuations. The avalanche size should follow a probability distribution. By assuming that the probability of ionization by an electron depends only on the electric field strength it can be described by the Furry distribution:

$$P(n) = \frac{e^{-n/\bar{n}}}{\bar{n}} \quad (3.14)$$

$\bar{n} = e^{-\alpha x}$ stands for the average avalanche size. Under the influence of a strong electric field, the probability of ionization cannot be treated as totally independent of its travelled path. So, the single-electron avalanche is expressed by the Polya distribution:

$$P(n) = C_0 \frac{(1+\theta)^{1+\theta}}{\Gamma(1+\theta)} \left(\frac{n}{\bar{n}}\right)^\theta \exp\left[-(1+\theta)\frac{n}{\bar{n}}\right] \quad (3.15)$$

where θ is the parameter related to the relative gain variance $f = 1/(1+\theta)$. Polya distribution can well describe the avalanche fluctuations in homogeneous fields and it lacks any physical interpretation.

During the avalanche process, electrons that gained enough energy can provoke excitations to the gas molecules, which then decay to their ground state through the emission of a visible or ultraviolet photon. However, these photons may create additional ionizations in the gas. The multiplication though cannot be increased up to the Raether limit for the avalanche size $\sim 10^8$ thus it will lead to a breakdown of the detector supplied voltage. The addition of a small amount of poly-atomic gas (quench gas) to many of the common gases used in gaseous detectors, can eliminate these processes by absorbing the photons.

Ionization can be also occurred by the energy excess of an excited state of a molecule or atom



3.2 Energy loss in thin absorbers

Bethe-Bloch equation gives only the average energy loss of a charged particle while traversing an absorbing medium. Detectors only measure the energy which is actually deposited in their sensitive medium. Any charged particle entering detector's volume immediately interacts simultaneously with medium's electrons through Coulomb forces. The products of these interactions are either excited atoms or electron-ion pairs. Sometimes, the electrons produced receive enough energy to incur further ionizations on their own. Secondary electrons are produced which with a certain probability may receive enough energy to produce ionizations on their own as well or even escape the detector's volume. These electrons are called δ -electrons and as explained above contribute to the energy which is actually deposited in detector's volume. As a result, for thin absorbers fluctuations around the average energy loss appear and they are due to δ -electrons. That asymmetric distribution can be parametrised by the Landau distribution.

3.3 Micromegas operation principle

Micromegas detectors consist of a planar (drift) electrode, a gas gap of a few micrometers thickness acting as conversion and drift region and a thin metallic mesh at typically $100 - 150 \mu\text{m}$ distance from the readout electrode, creating the amplification region. By the application of high voltages on detector's electrodes the electric field in the drift region is of the order of $\sim 0.6 \text{ kV/cm}$ and of $40 - 50 \text{ kV/cm}$ in the amplification region.

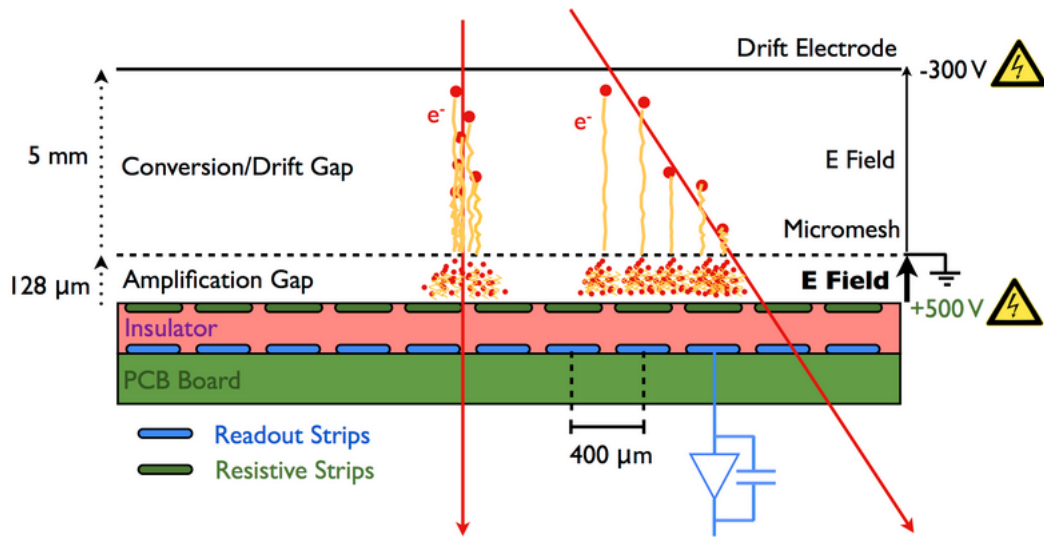


Figure 3.2: Schematic of Micromegas detector and its operation principle [29]

Charged particles (eg. cosmic-muons) traversing the drift region ionize the gas and the electrons liberated by the ionization process drift towards the mesh. Because of the strong electric field in the amplification gap the mesh is transparent¹ to more than 95% of the electrons. The electron avalanche takes place in the thin amplification region, resulting in a fast pulse on the readout electrode. The ions that are produced in the avalanche process move back to the micromesh with velocities about 200 times slower than the electrons. Most of the ions are rapidly collected by the mesh and only few survive and drift towards to the cathode electrode. The rapid recovery from space charge effects makes the detector tolerant to high particle fluxes.

3.4 Micromegas gas mixture

A suitable gas mixture permits the detection of particles. The mixture should fulfill a set of requirements depending on the purpose it is used for. Typically, it consists of a gas (most suitable are noble gases) in which ionization takes place and of another gas (most suitable are polyatomic gases as CO_2) which is used as a quencher to prevent secondary effects like photon feedback and field emission in order to get a stable gas gain well separated from the noise.

For the tracking at high values of luminosity the gas mixture has to compromise between a high drift velocity and a large primary ionization statistics. The drift velocity would ideally be saturated or have a small variation with modifications in electric and magnetic fields. As shown in Fig. 3.3, 3.4a, 3.4b the addition of the quench gas leads to higher drift velocities and reduced diffusions compared with the pure argon case.

¹The electron transparency of the mesh depends on the mesh characteristics and the ratio of the drift and amplification electric fields.

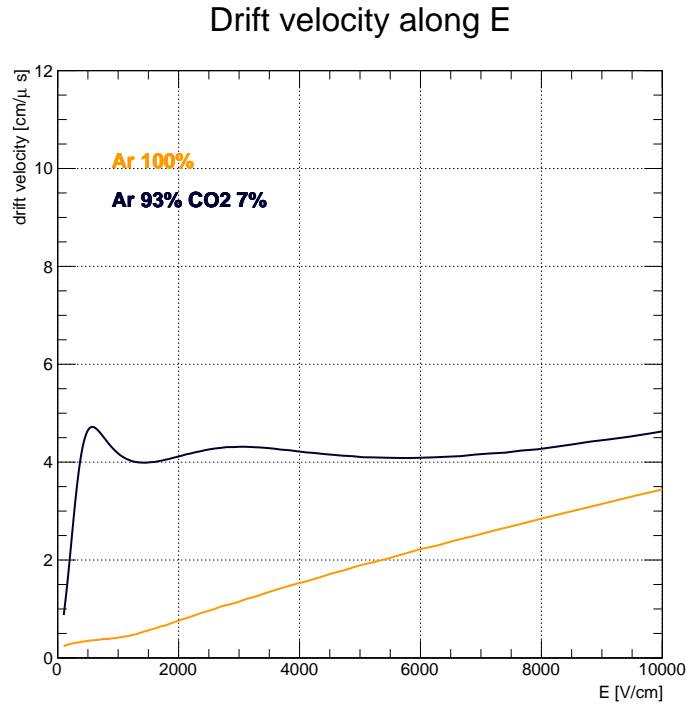
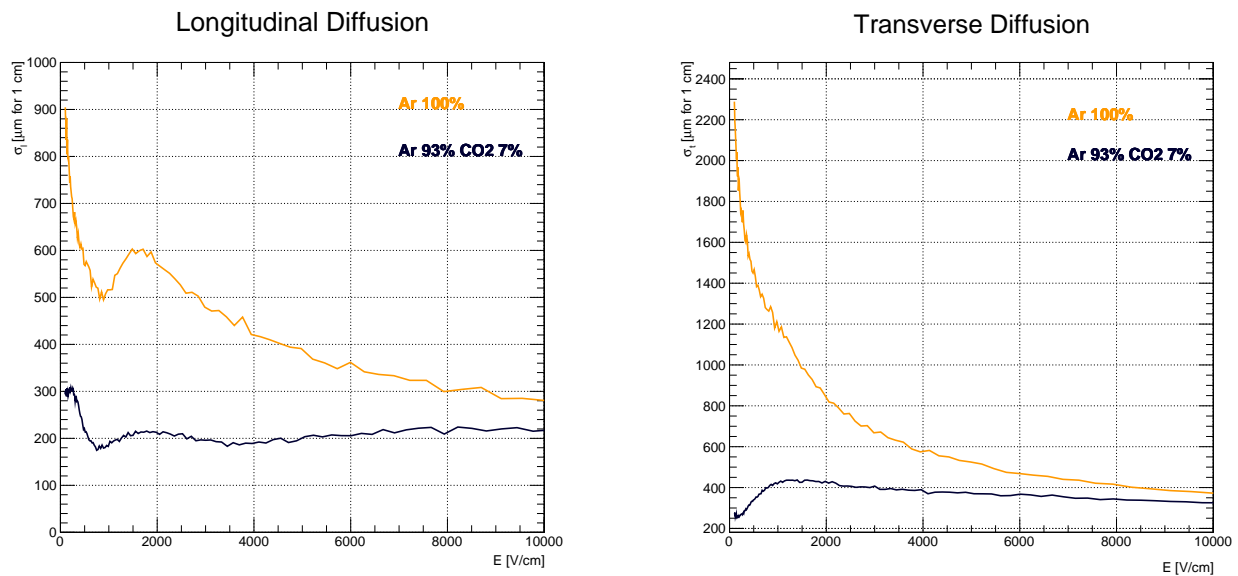


Figure 3.3: Drift velocity in pure argon and in Ar/CO₂ mixture. The distributions are computed using Garfield++ and Magboltz.



(a) Longitudinal diffusion in pure argon and in Ar/CO₂ mixture. The distributions are computed using Garfield++ and Magboltz.

(b) Transverse diffusion in pure argon and in Ar/CO₂ mixture. The distributions are computed using Garfield++ and Magboltz.

Figure 3.4

3.5 Simulation of Micromegas detector

A study for the Micromegas detector with the use of gmsh, ElmerFEM and Garfield++ software tools follows.

3.5.1 Gmsh



Gmsh is an open source mesh generator with a built-in CAD engine and post-processor which was developed by Christophe Geuzaine and Jean-François Remacle. Its design goal is to provide a fast, light and user-friendly meshing tool. The definition of the geometry can be evaluated either by using the graphical user interface or the text entry. The combination of both corresponds to the optimal way of the geometry's creation.

The user creates points and lines and then defines surfaces and volumes. Geometry specified in Gmsh is saved in a file with the extension .geo. After creating the geometry the procedure of meshing takes place. The finite elements' size is defined according to user's discretion. The finer the mesh the more precise the calculations and the calculation time is increased. At the command line

```
1. >> gmsh <filename>.geo -3 -order 2
```

a 3-dimensional mesh with tetrahedral elements suitable for second-order interpolation² is created which is saved in a different file with the extension .msh.

3.5.2 Elmer



Elmer is an open source multiphysical simulation software mainly developed by CSC-IT Center for Science (CSC). Elmer development was started in 1995 in collaboration with Finnish Universities, research institutes and industry for the purpose of solving partial differential equations by the finite element method. Elmer includes physical models for all branches of computational engineering and even beyond. Some application examples consist of fluid mechanics, structural mechanics, electromagnetism, acoustics, heat transfer, quantum chemistry, etc problems. The user can either use the graphical user interface or the text-entry format.

Elmer consists of the following sub-programs

1. ElmerGrid: meshing tool that can create simple structured 1D, 2D and 3D meshes of first, second and third order. The program can be used as a filter and converter for exporting, manipulating and transforming finite element meshes and file formats.
2. ElmerSolver: processes partial differential equations in a discrete form, handles coupled systems, non linearities and time-dependencies and generates output data for post-processing and visualization.
3. ElmerPost: visualization and post processing tool for the numerical results produced by ElmerSolver. It is capable of drawing contours, iso-surfaces, vector fields.
4. ElmerGUI: graphical user interface for defining and generating the input data for ElmerSolver.

The mesh output produced by Gmsh must be converted into a format readable by ElmerSolver with the use of the following command

```
2. >> ElmerGrid 14 2 <filename>.msh - autoclean
```

The options "14" and "2" indicate the input file (.msh - gmsh format) and the output file (.mesh* - ElmerSolver format) accordingly. The -autoclean option indicates that the physical elements defined in the geometry file will have their IDs re-numbered starting at 1. ElmerGrid should produce a folder which contains 4 output files (mesh.boundary, mesh.elements, mesh.header, mesh.nodes) all of them will be read by ElmerSolver and later by Garfield++.

The materials, the boundary conditions, the physical constants etc. are defined in a file with the extension .sif. By the following command

```
3. >> ElmerSolver <filename>.sif
```

two new files <filename>.result, <filename>.ep are created. The <filename>.ep file can be read by ElmerPost whereas the <filename>.result contains all the solution of the problem and is implemented in Garfield++ for the simulation part of the detector response.

²Only second-order gmsh-based meshes are currently supported in Garfield++.

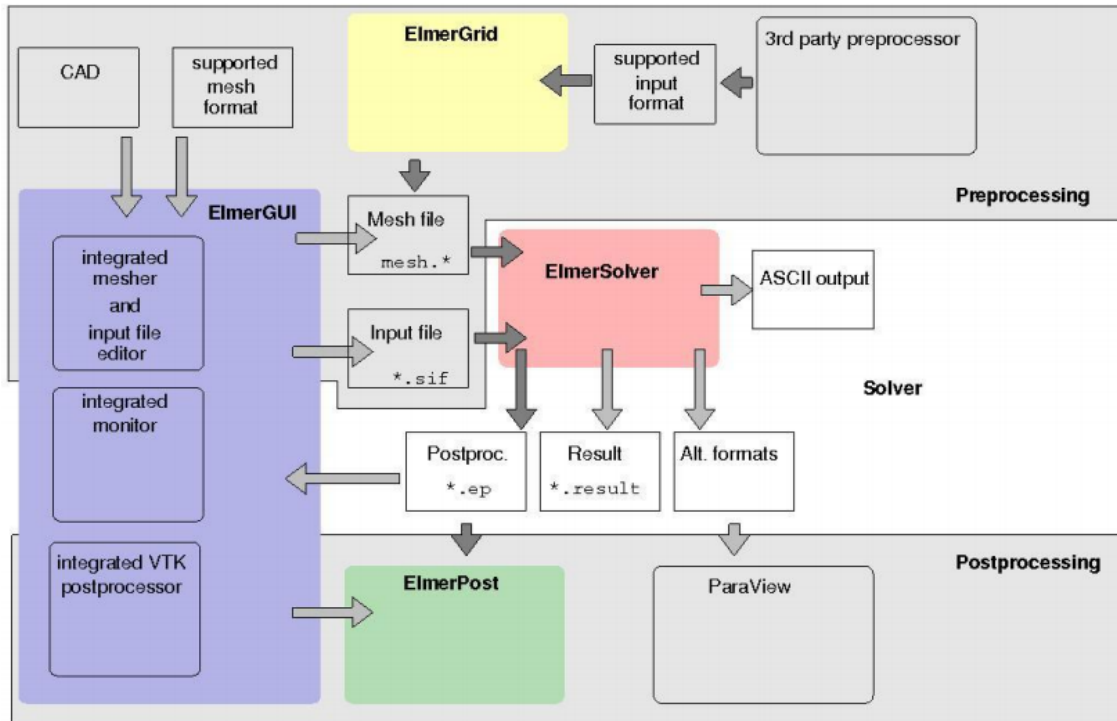


Figure 3.5: Elmer’s components

3.5.3 Garfield++



Garfield++ is an object-oriented tool for the detailed simulation of particle detectors that use a gas mixture or a semiconductor material as sensitive medium. It is the successor of Garfield, a toolkit that was developed at CERN in 1984 written in FORTRAN. On the other hand, Garfield++ is written in C++. The user, can construct and calculate the electric fields of simple geometries through this toolkit. However, for more precise simulations and for more detailed geometries Ansys, Synopsys TCAD, Elmer, CST, neBEM³ outputs can be implemented in Garfield++.

For the calculation of the transport properties of electrons in gas mixtures, an interface to the Magboltz program is available. For the simulation of the ionization produced along the track of relativistic charged particles an interface to the Heed program is available. Both of the above programs are developed at CERN.

There are two main categories of classes: classes that describe the detector (material properties, geometry, fields) and transport classes that deal with the tracking of particles through the device. The two class types are linked with the class Sensor. In addition, there are classes for visualization purposes that are based on the graphics classes of the ROOT framework.

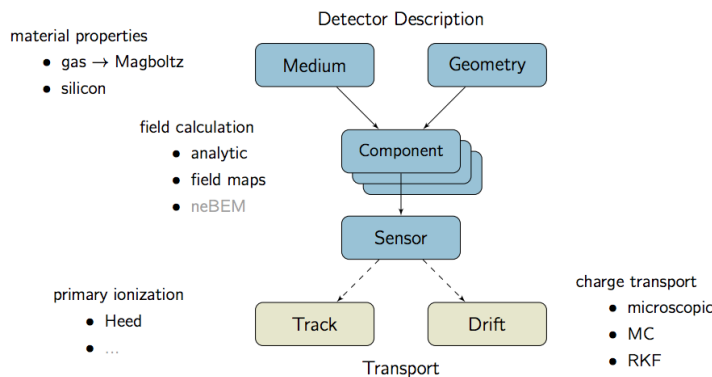


Figure 3.6: Garfield++ main classes

³In the future an interface to the neBEM field solver should be available. So far, such an interface is available for Garfield

Data analysis was developed with the use of ROOT framework.

3.5.4 ROOT



ROOT is an object-oriented tool developed in the middle of 90s aiming the particle physics data analysis at CERN. It contains several features specific to this field, but it is also used in other applications such as astronomy and data mining. It provides a graphical user interface and a GUI builder, a C++ script and a command line interpreter, CINT. Some of the packages provided by ROOT include those for

- histogramming and graphing in 2 or 3 dimensions.
- curve fitting
- four-vector computations
- 3D visualizations
- interfacing Python and Ruby
- interfacing Monte Carlo event generators
- creating files in various formats

3.6 Geometry and electric fields

Detector's geometry consists of 3 components:

1. the cathode
2. the micromesh
3. the anode strips

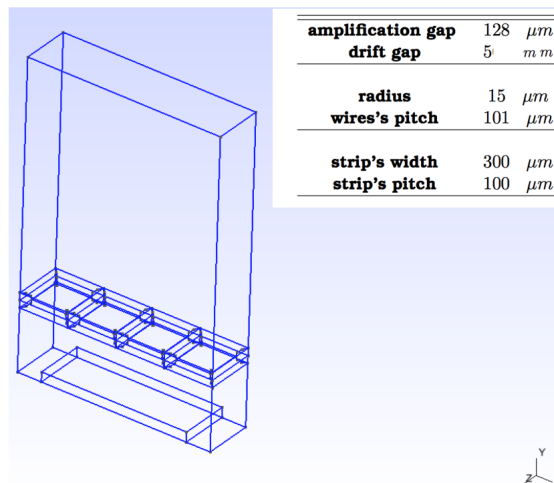


Figure 3.7: Geometry characteristics

Setting the appropriate voltage conditions on detector's components using Elmer, we have all the necessary file inputs for the simulation of detector's response.

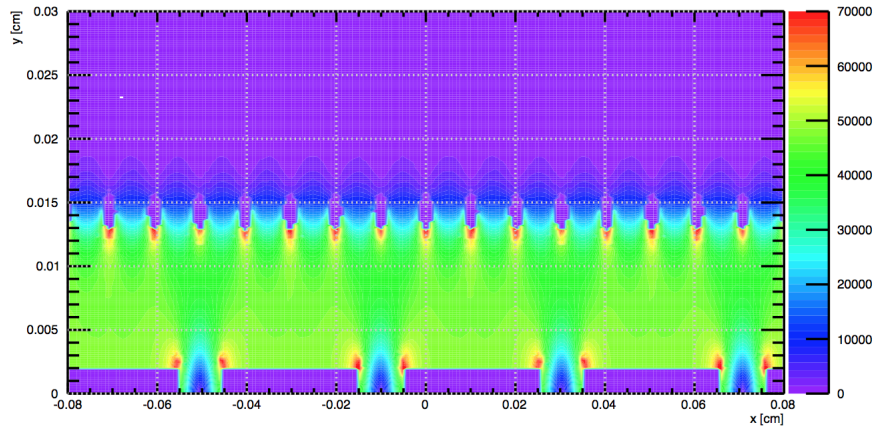


Figure 3.8: Contour plot of the electric field in the detector

3.6.1 Energy in drift region

Starting an electron of 0 eV at 5mm we get the following output for its energy distribution in drift region. The electric field in drift region is set at 0.6 kV/cm.

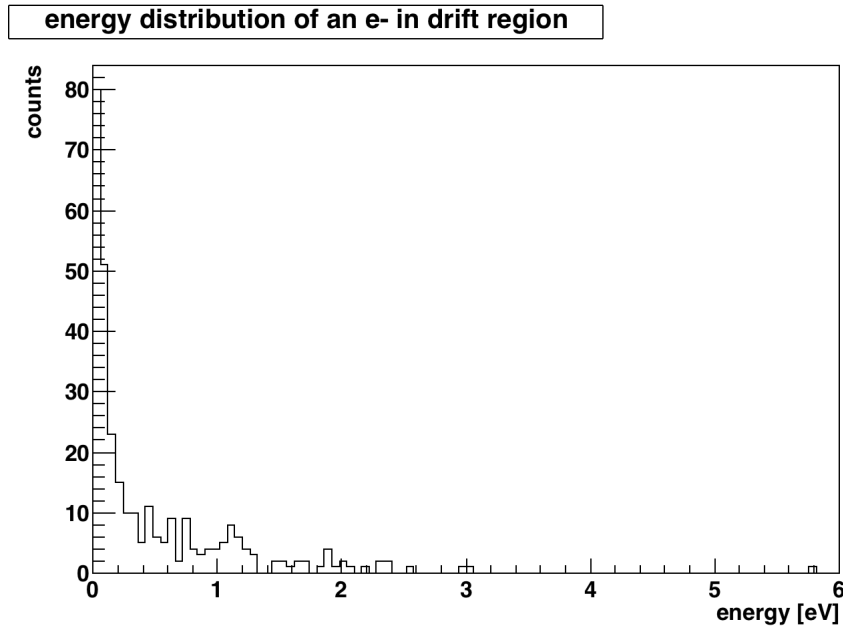


Figure 3.9: Energy distribution of 0eV electron in drift region

Because of the low electric field in drift region, electron's energy doesn't reach high values. When it reaches the mesh and goes into the amplification region the energy starts to increase giving rise to the avalanche effect.

3.6.2 Electrons starting with some energy

The study of electrons drifting in the detector with some initial energy is of a great importance. The ionization energy threshold values of Ar and CO₂ gases are 15.8eV and 13.8eV. Starting an electron with some energy can result in the birth of electrons, the number of them depending on the energy of the initial particle. The number of electrons in the amplification gap will be the result of the avalanche effect of maybe more than one electrons. In this section is presented the output of one run so as to get a general view. For a more detailed and precise output the statistics has to be increased.

| initial energy [eV] | #of e in drift region | #of e in amplification gap |
|---------------------|-----------------------|----------------------------|
| 0 | 1 | 7924 |
| 5 | 1 | 3268 |
| 10 | 1 | 9022 |
| 15 | 1 | 13247 |
| 20 | 2 | 17078 |
| 25 | 1 | 7646 |
| 30 | 2 | 22998 |
| 35 | 2 | 12668 |
| 40 | 3 | 34692 |
| 50 | 3 | 10199 |
| 100 | 4 | 31460 |

3.6.3 Presence of air in detector’s volume

The conditions in the detector volume are not optimal. As a consequence, it is of great interest to understand the detector’s response if a small amount of air impurities is introduced in the detector. To study this effect air is considered as a mixture of $N_2 : O_2$ (the other components are neglected) with a concentration of 79:21. Different fractions of air in the gas mixture were simulated. For the operating point 600V/cm, the addition of air results into reduction of the drift velocity and the transverse

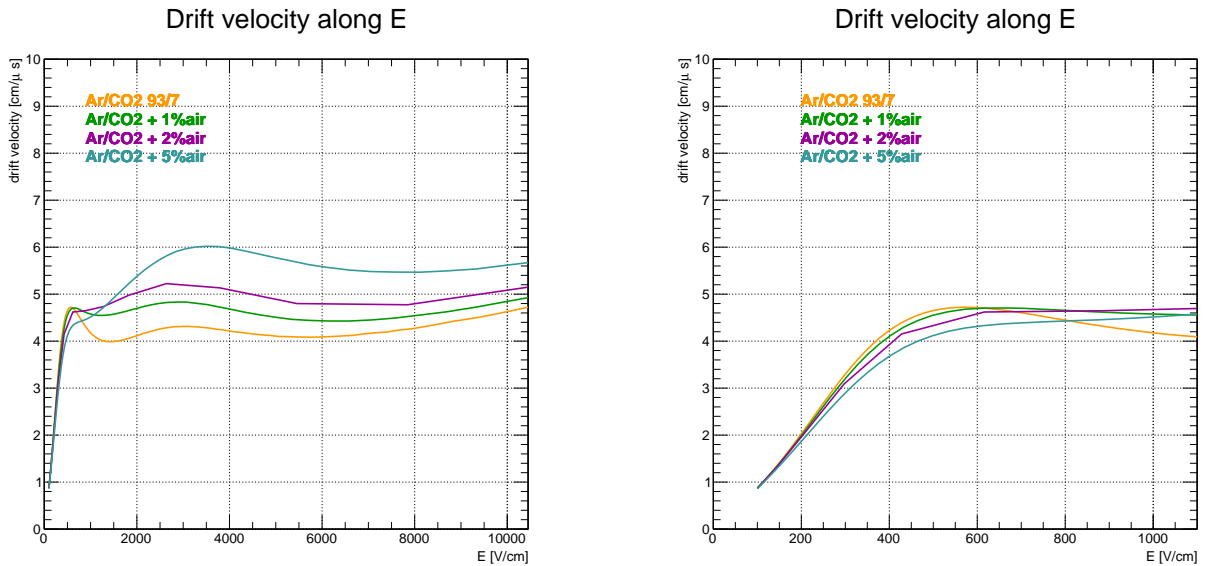


Figure 3.10: Drift velocity for different fractions of air

diffusion as the fraction of air increases. However, the longitudinal diffusion coefficient does not follow the same behavior.

Figure 3.13, 3.14 show the drift velocity and diffusion coefficients respectively as a function of the electric field for the cases of gas mixture Ar/CO₂ with one of air’s components. It is shown that the component that results in variations is the N_2 .

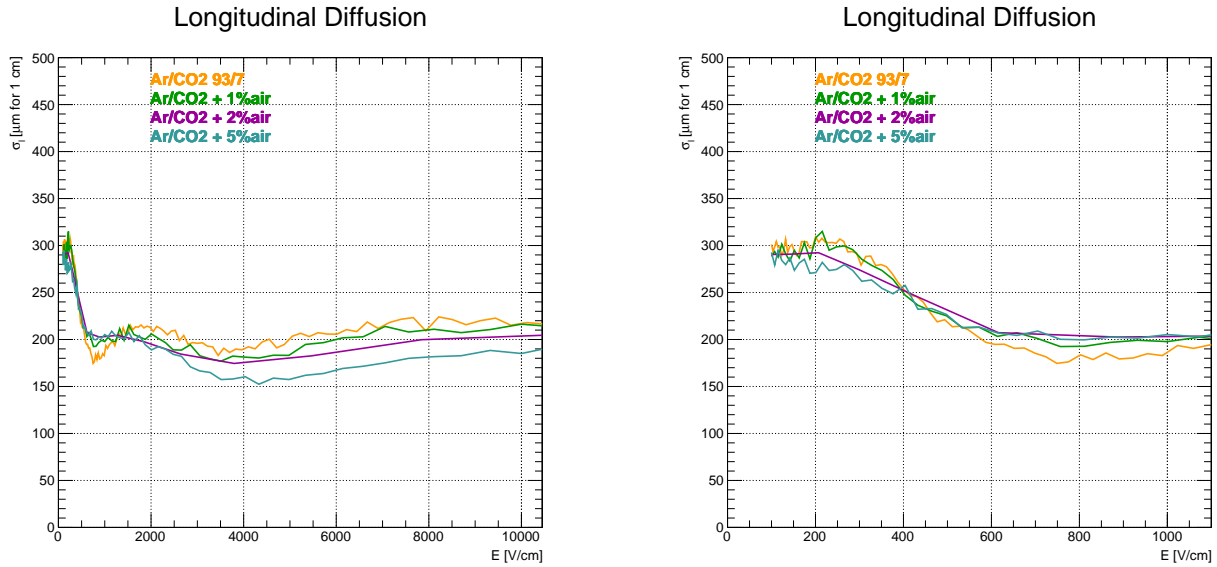


Figure 3.11: Longitudinal diffusion for different fractions of air

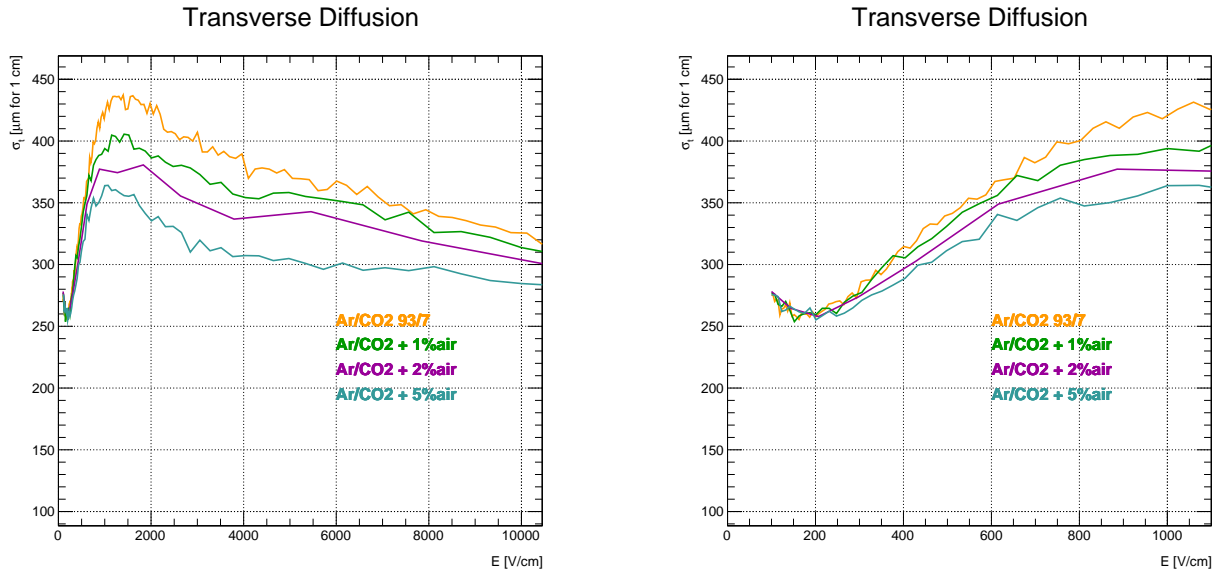


Figure 3.12: Transverse diffusion for different fractions of air

To obtain correct results from the simulation of the detector’s response the user has to find an optimal meshing size for the calculation of the electric fields and to set the correct value for the penning effect probability. The following results are obtained without taking into account the penning effect (in gas mixtures) and the meshing size is not good enough.

Drift velocity along E

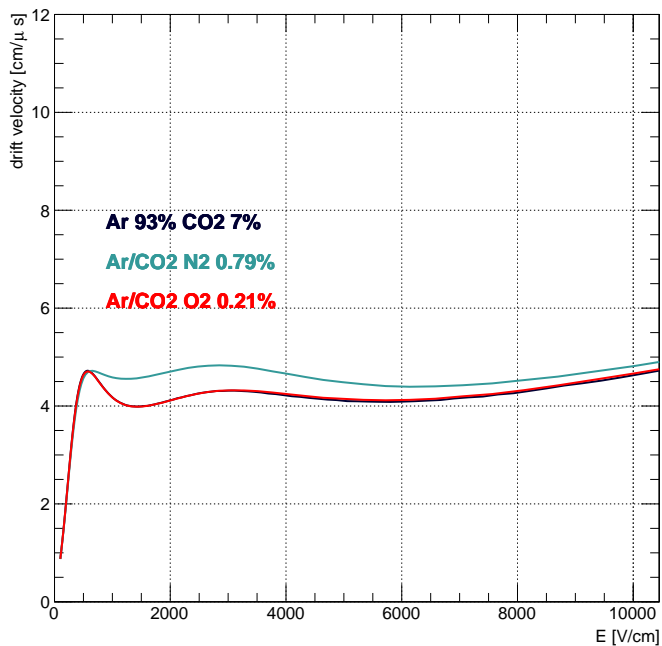
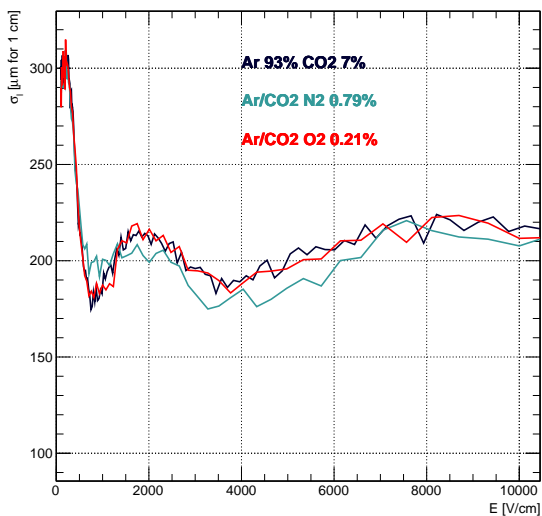


Figure 3.13: Drift velocity for Ar/CO2 93/7, Ar/CO2+0.79N2, Ar/CO2+0.21O2 mixtures

Longitudinal Diffusion



Transverse Diffusion

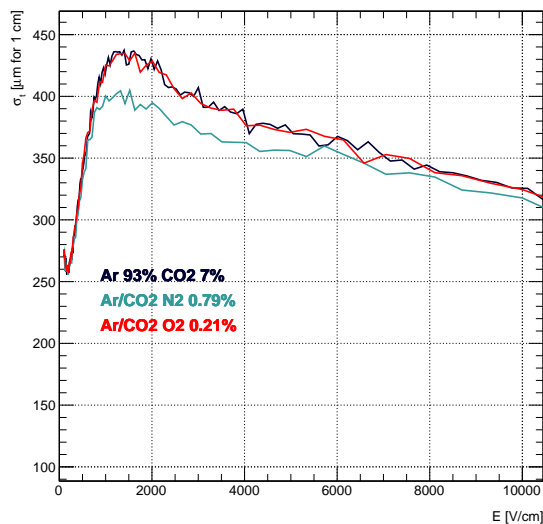


Figure 3.14: Diffusion coefficients for Ar/CO2 93/7, Ar/CO2+0.79N2, Ar/CO2+0.21O2 mixtures

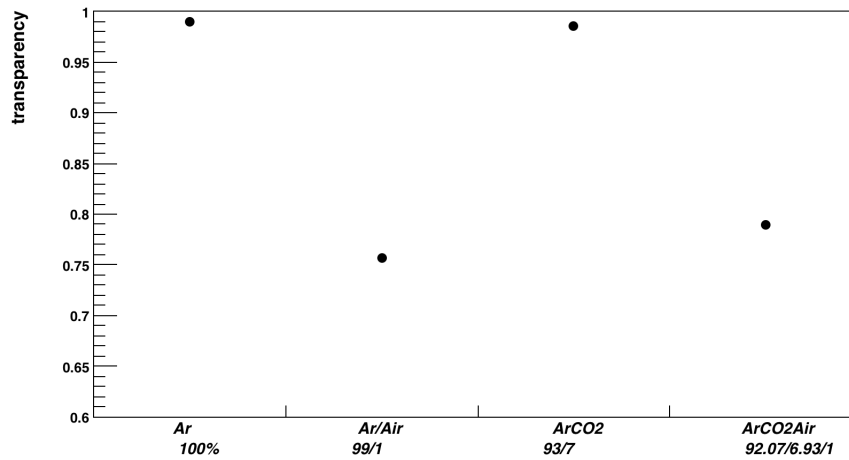


Figure 3.15: Mesh transparency for pure argon and Ar/CO₂ 93:7 compared with the case of air additions

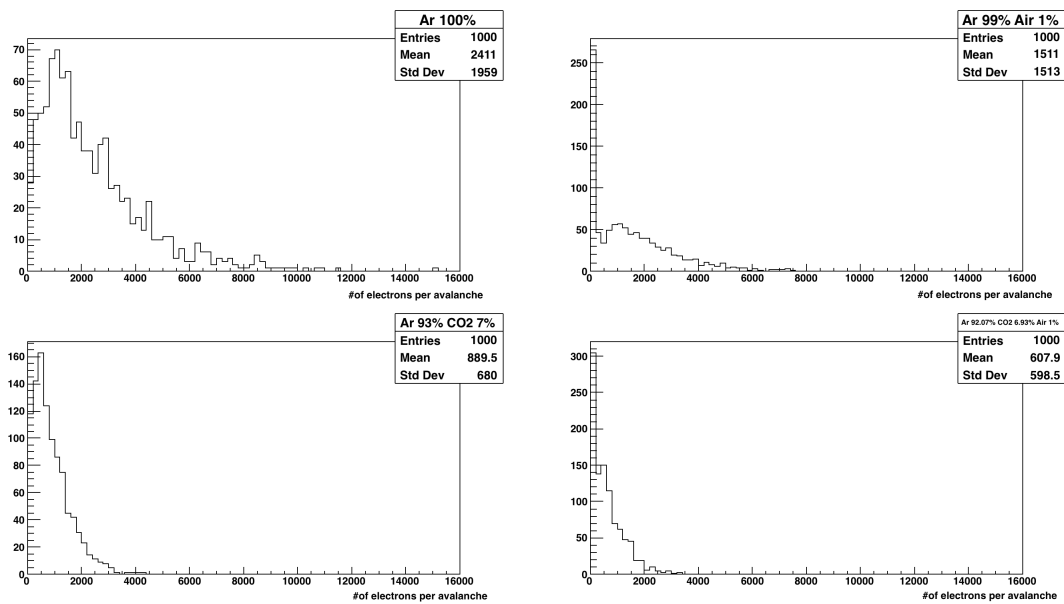


Figure 3.16: Distribution of the number of electrons produced by an electron in pure argon and Ar/CO₂ 93/7 compared with the case of air additions.

The presence of electronegative atoms like O_2 in the gas mixture reduces the detector's response because of their property of electron attachment. As mentioned in [32] 1% of air in argon will remove about 33% of the migrating electrons per cm of drift due to electron capture. Fig. 3.15 shows that the addition of air in Ar and Ar/CO₂ presents the same behavior in transparency. Fig. 3.17 presents the decrease of the transparency when small quantities of air are added in the gas mixture Ar/CO₂ 93/7 (for a finer meshing size).

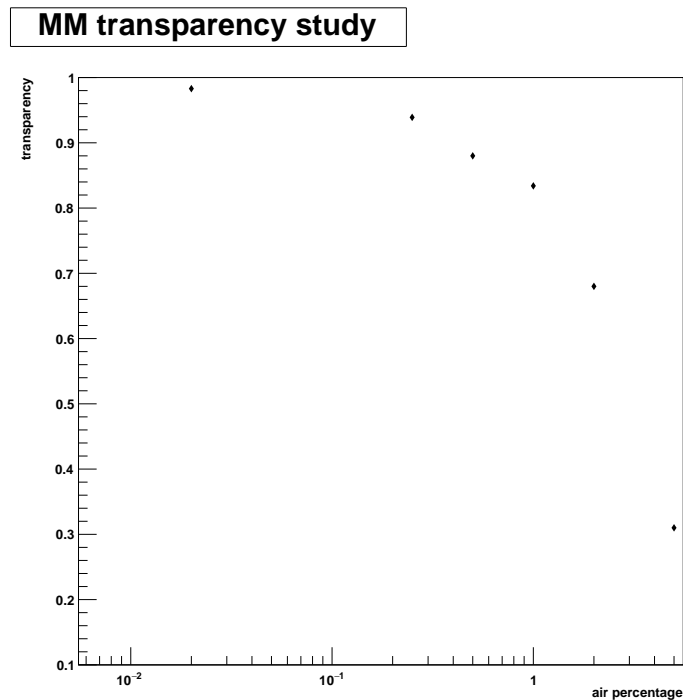


Figure 3.17: Transparency study for different air additions in the gas mixture Ar/CO₂ (finer meshing size).

3.7 Muon telescopes for volcano tomography

In order to produce shadow pictures of the interior of geophysical structures, measurements about the muon flux attenuation after crossing the target, are taken from the one side of the dome. Because of the reduced muon flux rate at large zenith angles (rare events), the useful information available requires long acquisition time.

An array of successive MicroMegas panels is capable to define and reconstruct muon trajectories. To detect muon tracks, at least two MicroMegas detectors are needed [30]. An arrangement with more detectors may be useful to better distinguish "fake" tracks coming from two charged particles interacting simultaneously in the two panels. Moreover, the distance at which the detectors will be placed has to be adjusted in order to adapt the total angular aperture [31].

The telescopes are intended to operate in harsh environments (higher temperatures which lead to higher pressures). Under such conditions, the avalanche size in the amplification gap is lowered [30] and a high performance of the readout electronics is of a great importance.

Some first measurements have to be realized in open sky conditions to calibrate the set-up and to measure the environmental fluctuations [31].

Multiplexing is the method by which multiple analog message signals or digital data streams are combined into one signal over a shared medium (from: wikipedia). The reconstruction of the muon tracks is realized through the reverse process (demultiplexing) [30]. The information about the muon position in the detector volume lead us to the muography of the geophysical edifice.

Simulation study of volcano radiography with muons

This chapter deals with the interaction of muons with matter through Monte-Carlo simulations. The simulation studies were carried out using the GEANT4 simulation platform.

Geant 4 (GEometry ANd Tracking) is an open source toolkit for the simulation of the passage of particles through matter using Monte Carlo methods. It is the successor of the GEANT (written in FORTRAN) developed by CERN. Geant4 is a complete rewrite in C++ with a modern object-oriented design. Its development, maintenance and user support are taken care by the international Geant4 Collaboration. Its areas of application include high energy, nuclear and accelerator physics, as well as studies in medical and space science.

The user can develop its own virtual experiment with a great success. The facilities the package offers are listed below:

1. Geometry: an analysis of the physical layout of the experiment including the materials used
2. Tracking: simulation of particles and their passage through matter considering possible interactions and decay processes
3. Detector response: an approximation of how a real detector would respond when a particle passes through its volume
4. Run management: all the useful information of each run is extracted
5. Visualization: user interface based on Tcsh and a number of options including OpenGL is offered

Classes at the bottom of the diagram are used virtually by all higher classes and provide the foundation of the toolkit. Global classes covers the system of units, constants, numerics and random number generators. Materials and Particles modules offer the description of the physical properties of particles and materials for the simulation of particle-matter interactions whereas Geometry category implements the description of the geometrical structure and enables the particles to propagate efficiently through it. Track contains classes for tracks and steps used by the Processes category which implements the physics models. All processes are invoked by the Tracking category which manages their contribution of a track's evolution and provides information in sensitive volumes for hits and digitization. Above these, the Event classes manage the events in terms of their tracks and Run classes manage the collection of events that share a common beam and detector implementation. Readout module handles all the information that is produced. Finally, Visualization, Persistency and Interface categories connect the toolkit with the user by providing a command-line interaction and the visualization of the experiment.

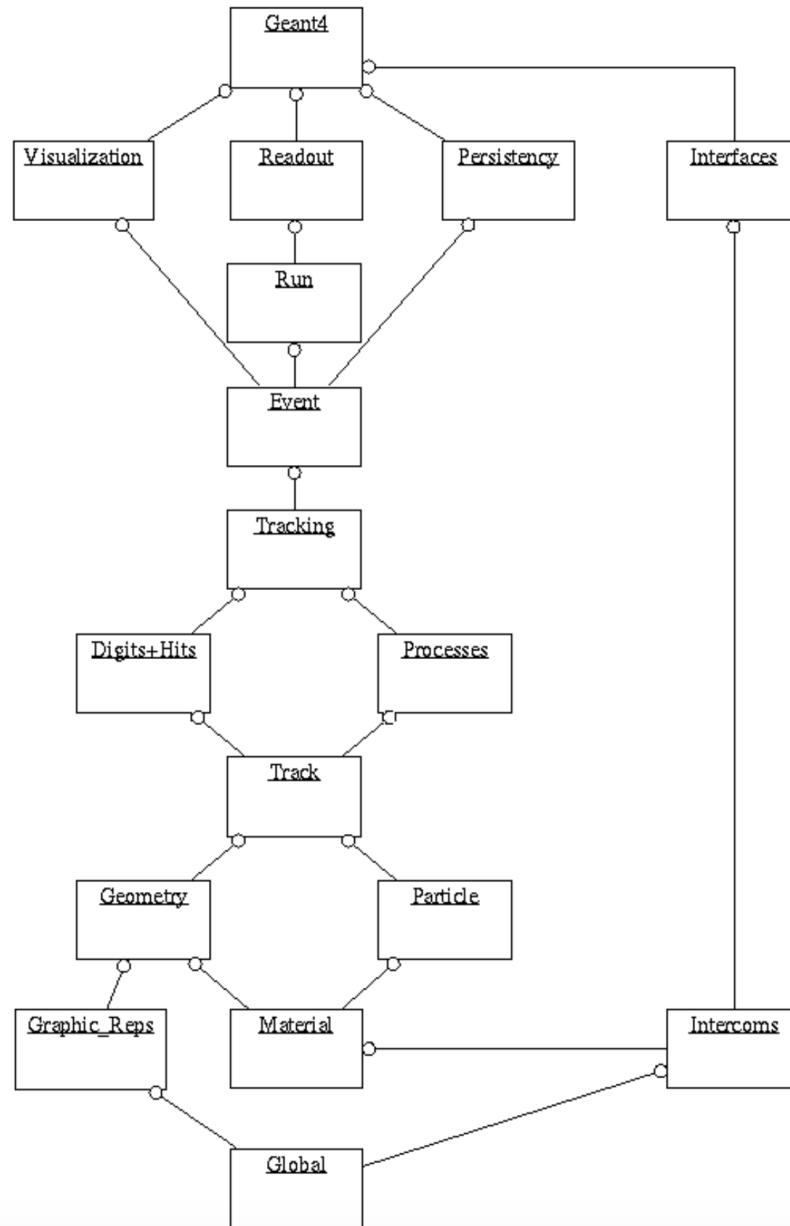


Figure 4.1: Geant4 classes diagram

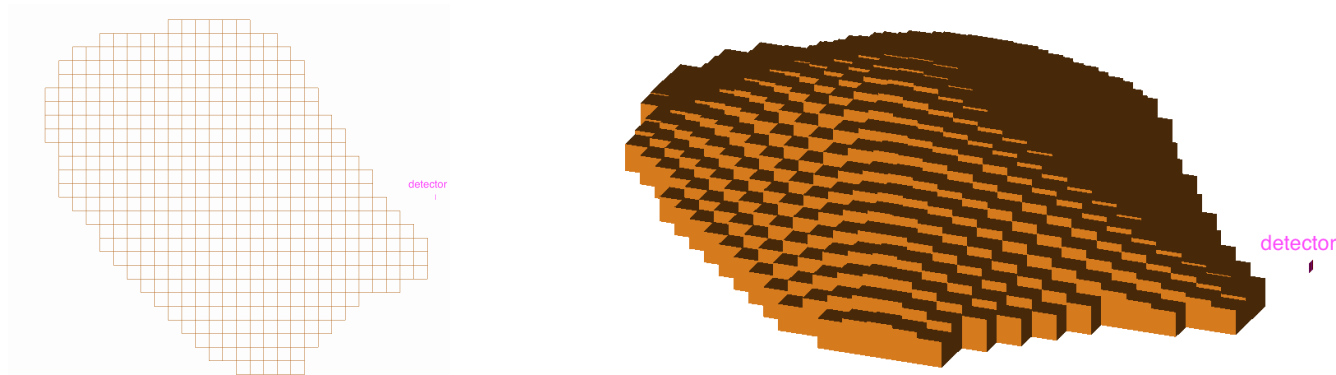


Figure 4.3: Schematic view of the geometry. Left: Top view. Right: Side corner view.

4.2 Muon source

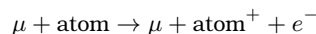
Simulation of cosmic muon-showers in Geant4 is a rather complicated task. Geant4 makes available 2D and 3D radiation sources that are defined by regular geometric shapes (eg. circle, ellipse, sphere, ellipsoid, cylinder, etc) only. The homogenous radiation field produced by such sources fails to represent the flux distribution of the secondary cosmic rays impinging on the Earth's surface. On the other hand, muography of volcanoes mostly takes advantage of nearly horizontal muon rays [24] ($> 80^\circ$ from zenith) as the vertical muons are attenuated more strongly. Hence, the Monte Carlo simulation was here based on the assumption that the detector would collect only horizontal muons, passing through the volcano, and the source was designed as muon beams of different energies. The energy values were based on the energy loss and range of muons in rock.

4.3 Coulomb Interactions

4.3.1 Energy loss and range study

The knowledge of the parameters of the transmission and absorption of muons in rock is of great importance for the experiment. By measuring the differential attenuation of the muon flux as a function of the amount of rock crossed along different directions, it is possible to determine the mean density of the interior of a volcano. In addition, it is useful in understanding their interaction with rock. An attempt to extract all the useful information about muon energy loss and range in rock, was made (Fig. 4.5, 4.6).

While passing through matter, muons interact with the material's atoms, losing gradually energy during several processes. The basic mechanism is the inelastic collision of the muon with the atomic electrons of the material, removing an electron from the atom (ionization) through the following process:



In each individual collision the energy transferred to the electron is small.

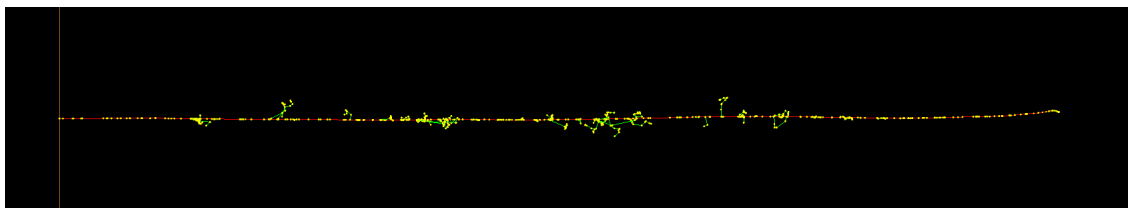
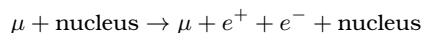


Figure 4.4: Muon track (red) of 4 GeV in rock. Green tracks refer to neutral particles. The muon experiences 275 ionizations and its range is about 8.07 m.

At high energies, radiative processes become more important than ionization. One of the most important processes is the direct pair production by muon:

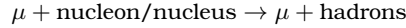


The average energy loss for pair production increases linearly with muon energy, and in TeV region contributes over 50% to the total energy loss rate.

A fast moving charged particle is decelerated in the Coulomb field of atoms (bremsstrahlung effect). A fraction of its kinetic energy is emitted in form of real photons. The average energy loss per unit path length due to the bremsstrahlung increases

linearly with the initial energy of the particle. In TeV region, this process contributes about 40% to the average muon energy loss.

In the high energy region, photonuclear reaction (production of charged hadrons by muons)



contributes about 10% of the total energy loss and it increases linearly with muon energy as well.

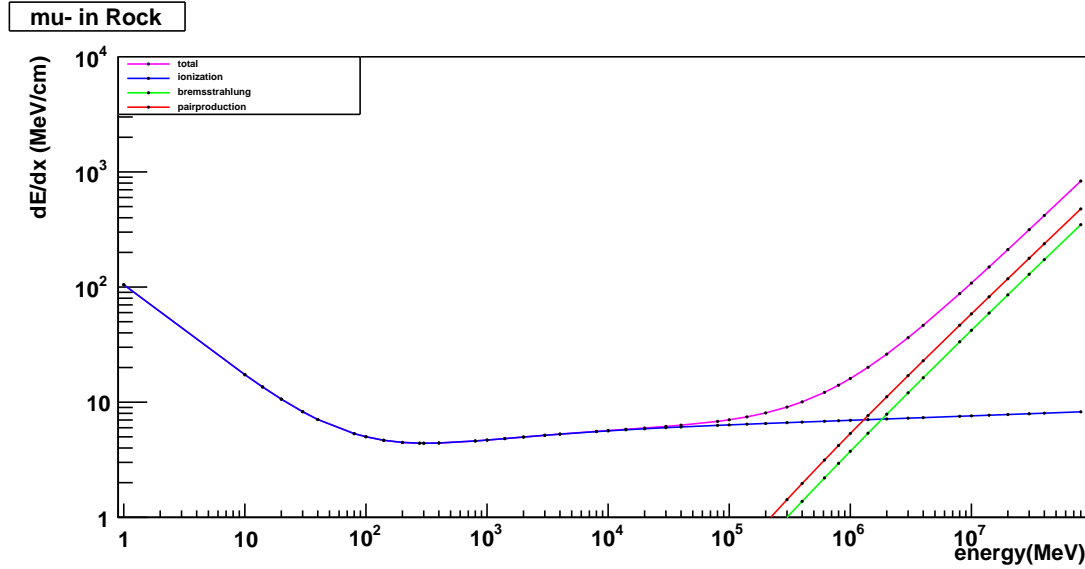


Figure 4.5: Simulation result for muon energy loss in rock. Magenta line: Total energy loss, Blue line: Ionization component, Red line: Pair production component, Green line: Bremsstrahlung component

The energy at which radiative and ionization losses are equal is called critical energy. For muons in rock the critical energy is estimated at ~ 773 GeV without taking into account the contribution of photonuclear interaction.

The range of muons in rock, is calculated by CSDA approximation and is shown in Figure 4.6.

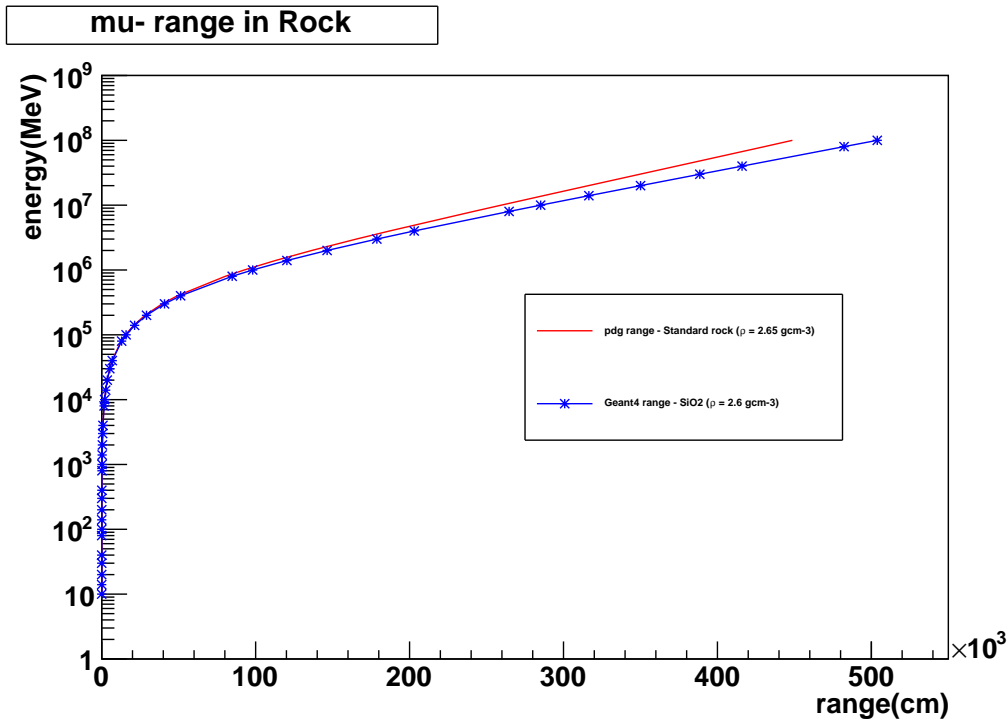


Figure 4.6: Simulation result for muon range in rock.

4.3.2 Scattering study

By knowing the muon ranges in rock it is possible to estimate the energies with those a muon can cross the whole dome. Only the case of horizontal muons ($\theta = 90$ deg) is studied. Muon tracks are generated on the one side of the volcano and at the other side the detector is placed. The dimensions of the detector simulated here do not correspond to the actual ones, as for scattering study applications the detector's size has to be larger than target's extent. Every muon has to transverse a huge volume of material. Along its path it experiences small deviations from its initial direction due to scattering and while it exits the absorber, it may not reach the detector volume. So, most of the events will be lost. Setting the detector volume as sensitive, information about the position in the volume is extracted (Fig. 4.7). Having all the appropriate data one can estimate the scattering along zenith and azimuth angles as

$$\Delta\theta = \arctan\left(\frac{y' - y_0}{z' - z_0}\right), \quad \Delta\phi = \arctan\left(\frac{x' - x_0}{z' - z_0}\right)$$

where x_0, y_0, z_0 are the coordinates of muons' initial position and x', y', z' the coordinates of muons' in the detector volume.

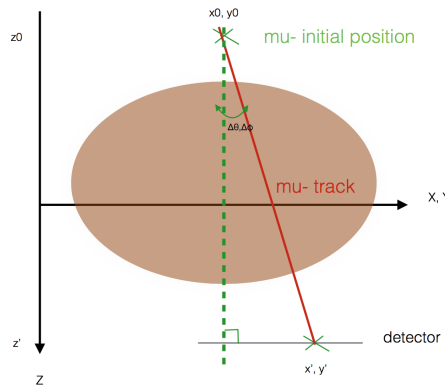


Figure 4.7: Schematic of the method used for the calculation of scattering angles

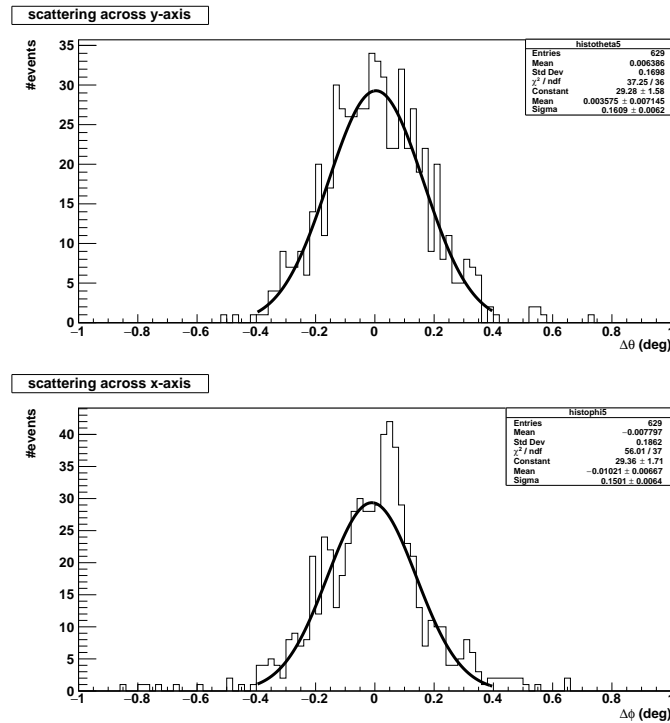


Figure 4.8: Scattering effect for 1k muons with energies of 500 GeV.

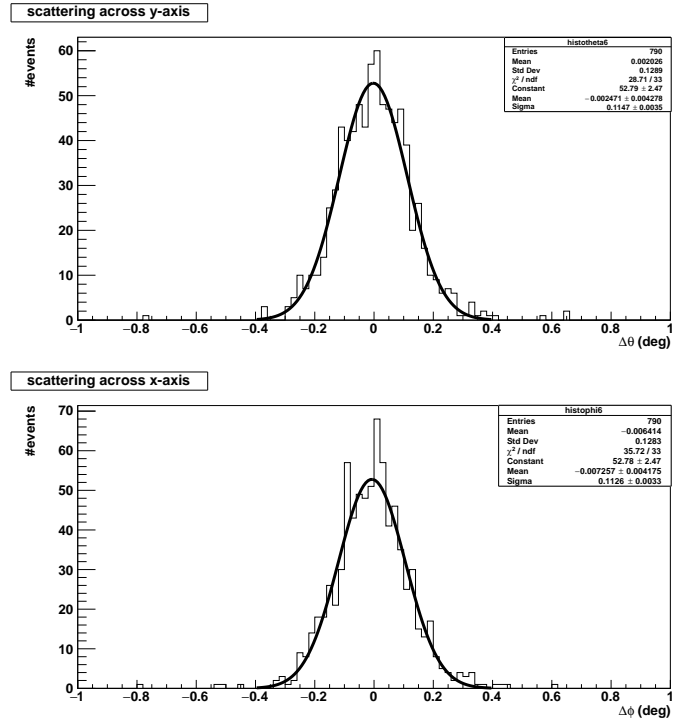


Figure 4.9: Scattering effect for 1k muons with energies of 600 GeV.

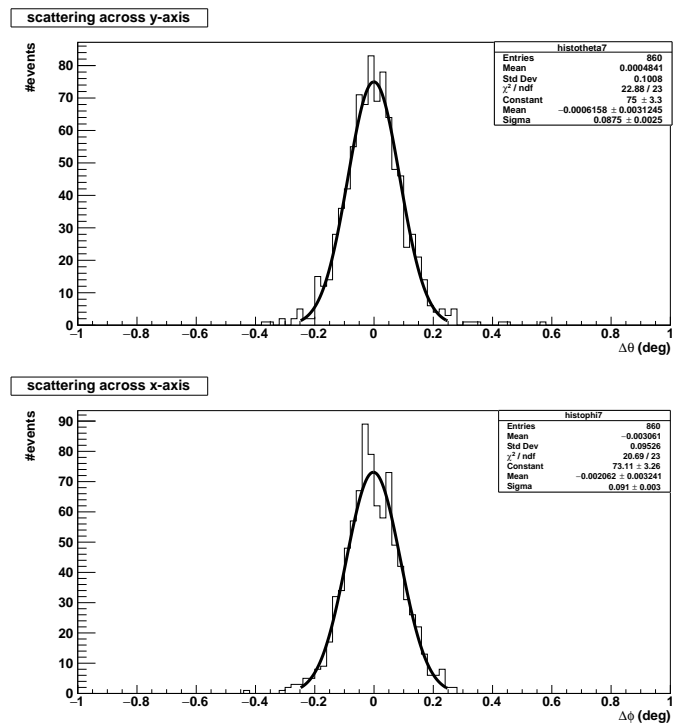


Figure 4.10: Scattering effect for 1k muons with energies of 700 GeV.

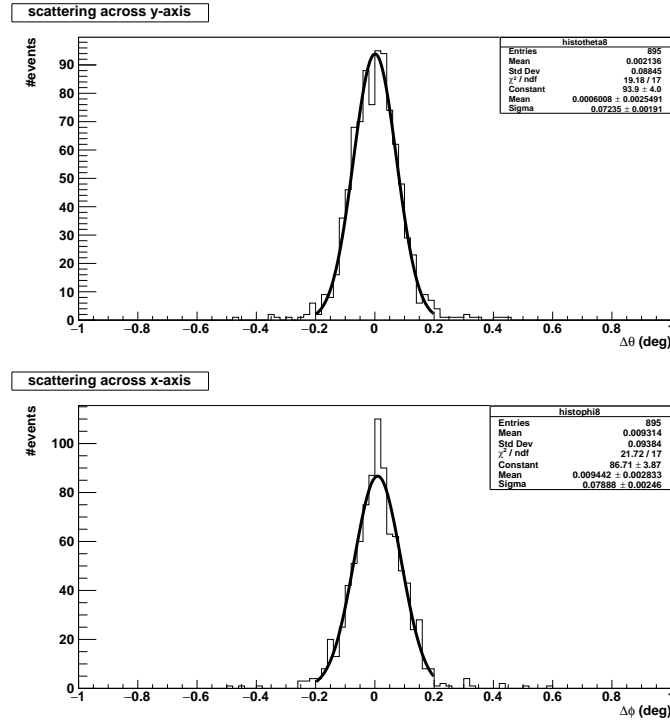


Figure 4.11: Scattering effect for 1k muons with energies of 800 GeV.

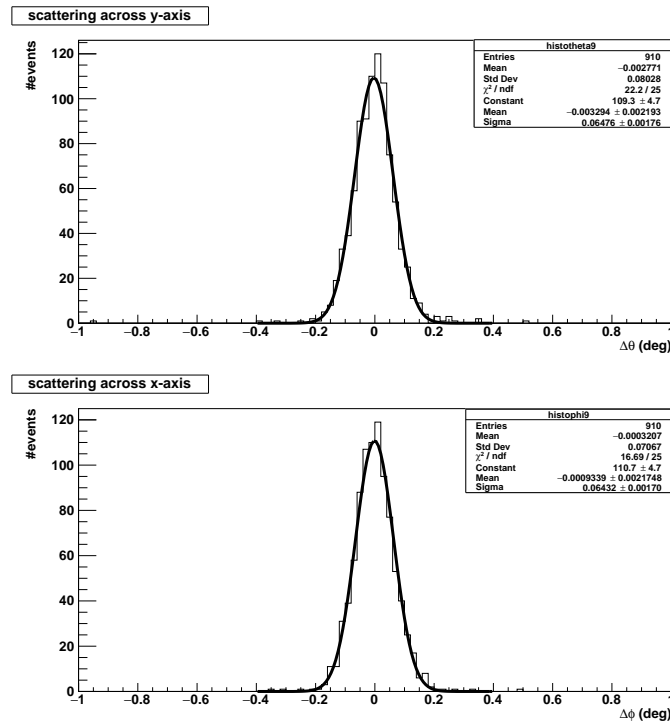


Figure 4.12: Scattering effect for 1k muons with energies of 900 GeV.

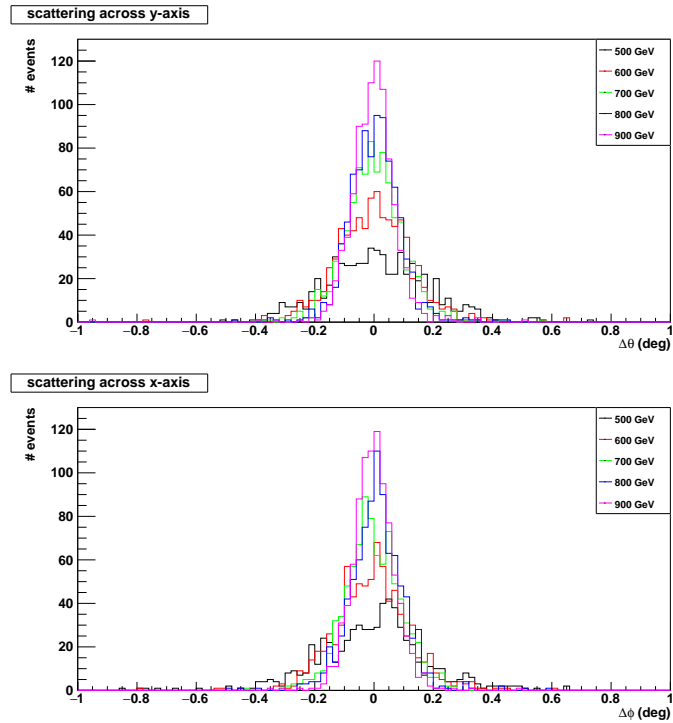


Figure 4.13: Distributions of scattering angles for different energies. Stacked histograms Fig. 4.8 - 4.12

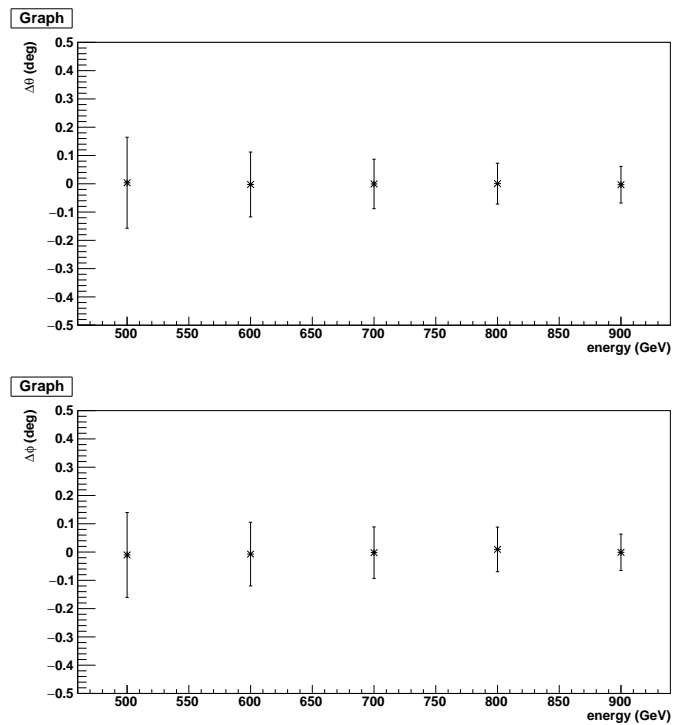


Figure 4.14: Distribution of scattering angles as a function of muon's energy.

The higher the initial muon's energy is, the steeper the peak of the distribution is and the more precise the calculation of the scattering effect becomes. The deviation on both zenith and azimuth angles of the initial muon's track after passing the volcanic dome is almost the same for all energy cases due to the symmetric path in the target it tranverses.

The scattering effect is studied again by a different approach. The detector's volume is divided into a number of pixels each of them is defined as sensitive. By changing the pixels' dimensions and the number of the initial generated events, we take the below outputs for horizontal muons of 900GeV.

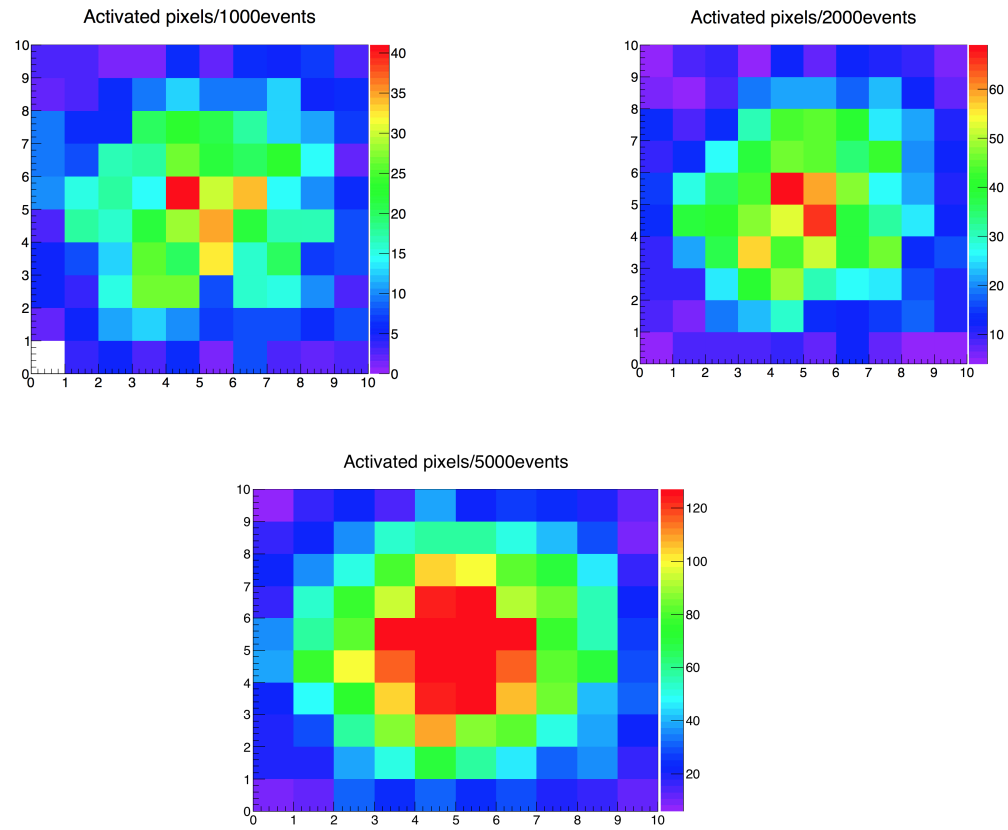


Figure 4.16: Scattering effect. The detector volume is divided into 1x1 m pixels. Top Left: 1000 muons with initial energy of 900GeV. Top Right: 2000 muons with initial energy of 900GeV. Bottom: 5000 muons with initial energy of 900GeV.

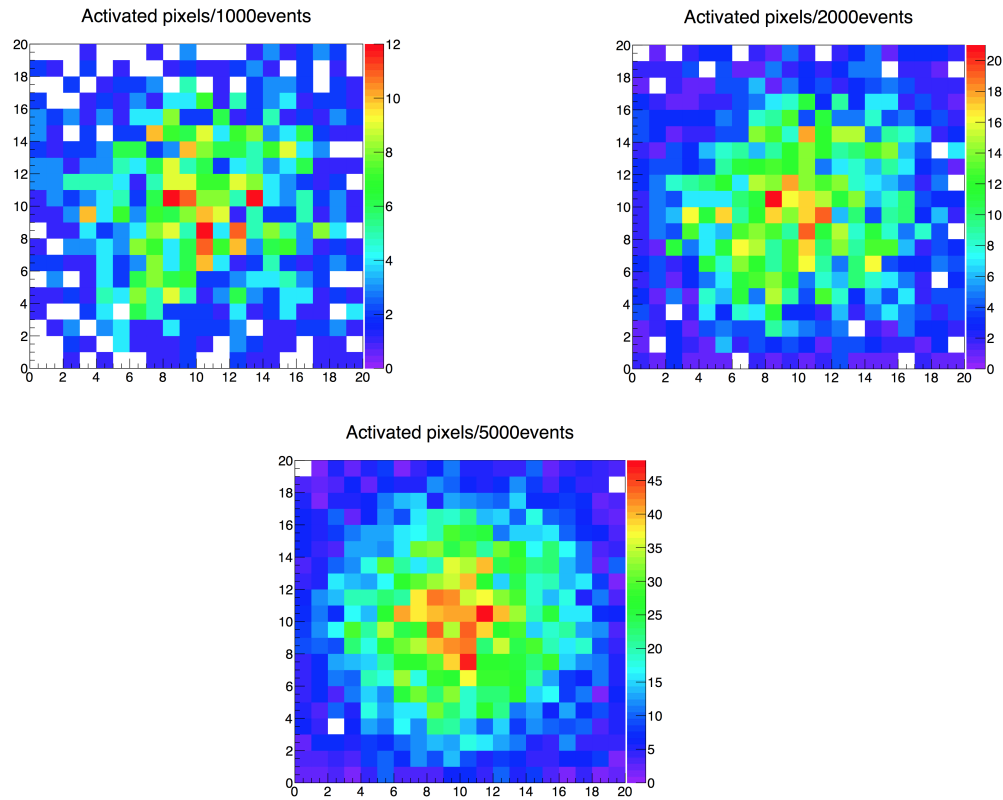


Figure 4.18: Scattering effect. The detector volume is divided into 0.5×0.5 m pixels. Top Left: 1000 muons with initial energy of 900GeV. Top Right: 2000 muons with initial energy of 900GeV. Bottom: 5000 muons with initial energy of 900GeV.

By increasing the number of initial events (which corresponds to higher exposure time) the more data we collect and the more precise becomes the output. At the same time, by changing the pixels' dimensions the output image is more detailed.

4.4 Energy distribution in detector

After crossing the volcano muons reach the detector, interact with the gas and leave a fraction or all of their energy in detector's volume. The energy distribution of muons with initial energy of 500, 600, 700, 800, 900 GeV in the detector is presented in the following plots and it is a result of all the particles that are maybe produced in the detector (ex. electrons, pions etc).

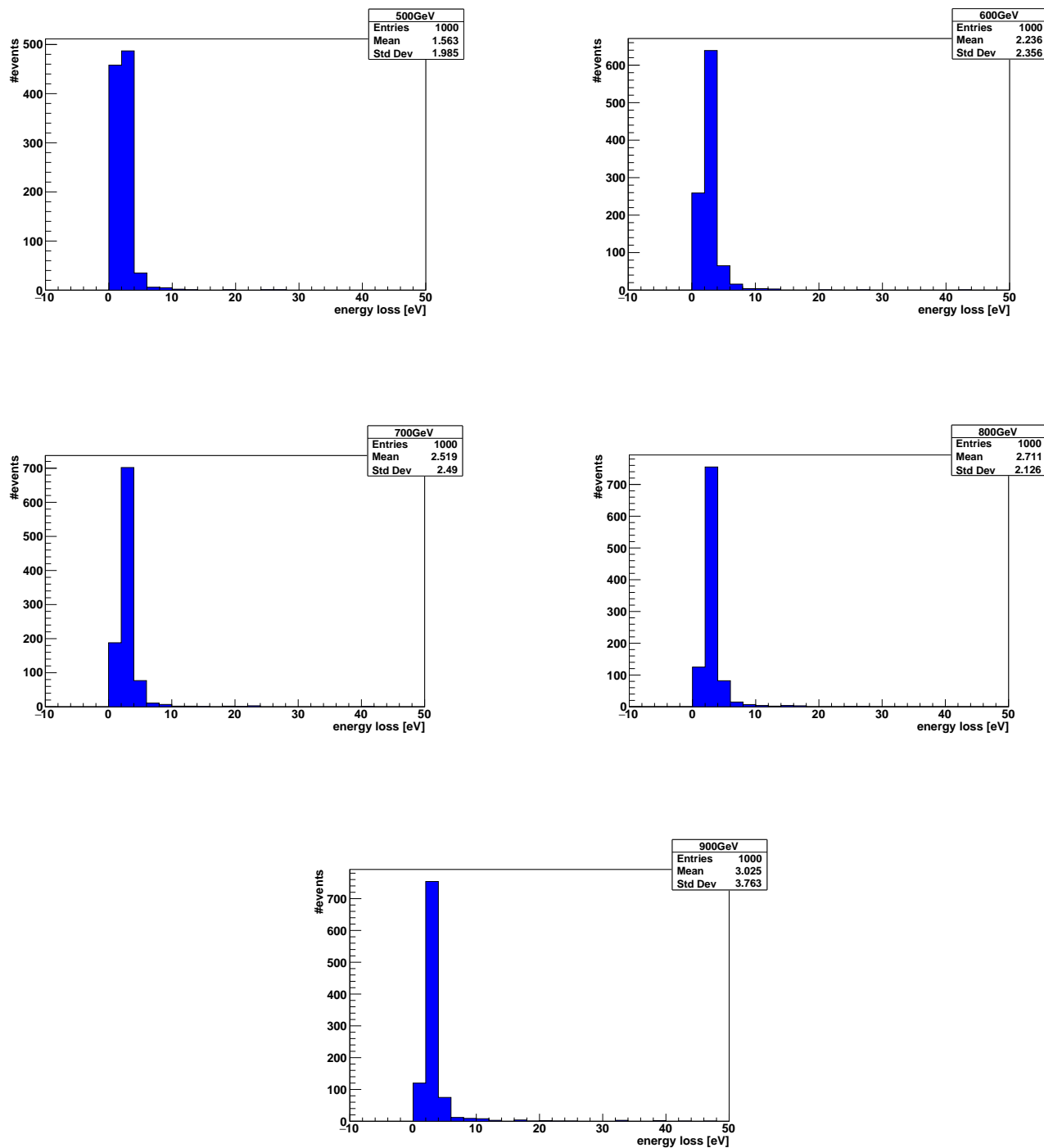


Figure 4.21: Energy distribution, in detector, of muons of different initial energy after crossing the volcano

Conclusions and future directions

In the first part of this master thesis the MicroMegas detector simulation response was presented. The construction of the detector's geometry as well as the calculation of the electric fields inside the detector's volume were evaluated using gmsh and ElmerFEM software tools respectively. Interfacing the above results into garfield++ detector physics simulation toolkit and with the use of Magboltz program electron transport properties for the typical gas mixture Ar/CO₂ 93/7 used in MicroMegas detectors were computed for different percentages of air impurities. The main goal was the examination of the detector's performance in the presence of small amounts of air in the volume. For this purpose, a study concerning the transparency and the gain of the detector in such conditions was performed.

The second and the last part of this thesis proposes the MicroMegas detectors for applications in volcano radiography with cosmic ray muons. At first, the average energy loss as well as the range in rock target of a density of 2.6 g/cm³ for muons were examined. The selection of the volcano dome under study was based on symmetry facts. Eventually, we concluded in one of the volcanic domes of Methana peninsula. The geometry was constructed in Geant4 simulation platform as a number of voxels. Data were retrieved by satellite imagery techniques that are freely available on the web. For the above mentioned geometry, a study for the scattering effect, for the case of horizontal muons only, after passing the edifice and the distribution of their energy in the detector was made.

Next plans for a further and a more precise analysis can contain an accurate creation of the cosmic-ray shower in Geant4 to obtain the real flux of muons after passing the dome. From the experimental point of view, a detailed layout of the detectors that will be used has to be examined so as to get experimental data and then compare them with the simulation output. Further simulations on the detector response concerning the gas anomalies on temperature and pressure will be proved really helpful.

List of Figures

| | | |
|------|---|----|
| 1.1 | Left: Earth's magnetic field, Right: The direction of motion of a positively and a negatively charge in the presence of magnetic field[1] | 4 |
| 1.2 | Development of a shower in matter through successive events of pair-production and radiation [1] | 5 |
| 1.3 | Experimental arrangement used by Street and Stevenson to obtain pictures of low-energy penetrating particles [1] | 5 |
| 1.4 | Photomicrograph of tracks in a nuclear emulsion [1] | 6 |
| 1.5 | Vertical intensity of three components of local cosmic radiation as a function of atmospheric depth in grams per square centimeter. Curve NA: nuclear-active particles with energies greater than about 1BeV. Curve E: electrons with energies greater than about 100 MeV. Curve M: muons with energies greater than about 200 MeV. | 6 |
| 1.6 | Composition of primary cosmic radiation [1] | 7 |
| 1.7 | Progeny of a cosmic-ray particle. The primary particle (usually a proton) collides with a nucleus of oxygen or nitrogen in the atmosphere. Its products as well as their interactions are depicted. [1] | 7 |
| 2.1 | Left: Vertical muon flux at sea level. Solid line: calculated by Lipari (Lipari, 1993). Dashed line: calculated by [4]. Data: Allkofer et al., 1971. Right: Zenithal ($\theta = 89^\circ$) muon flux at sea level. Solid line: calculated by Lipari (Lipari, 1993). Dashed line: calculated by [4]. Data: Matsumo, 1984. | 10 |
| 2.2 | Angular distribution of muons at sea level for different muon energies [5]. | 11 |
| 2.3 | Multiple Coulomb scattering (from: meroli.web.cern.ch) | 11 |
| 2.4 | Sketch of the muon radiography principle[16] | 14 |
| 3.1 | Left: Avalanche creation in a cloud chamber [33]. Right: Schematic view of the drop-like shape of an avalanche formation. | 17 |
| 3.2 | Schematic of Micromegas detector and its operation principle [29] | 18 |
| 3.3 | Drift velocity in pure argon and in Ar/CO2 mixture. The distributions are computed using Garfield++ and Magboltz. | 19 |
| 3.4 | | 19 |
| 3.5 | Elmer's components | 21 |
| 3.6 | Garfield++ main classes | 21 |
| 3.7 | Geometry characteristics | 22 |
| 3.8 | Contour plot of the electric field in the detector | 23 |
| 3.9 | Energy distribution of 0eV electron in drift region | 23 |
| 3.10 | Drift velocity for different fractions of air | 24 |
| 3.11 | Longitudinal diffusion for different fractions of air | 25 |
| 3.12 | Transverse diffusion for different fractions of air | 25 |
| 3.13 | Drift velocity for Ar/CO2 93/7, Ar/CO2+0.79N2, Ar/CO2+0.21O2 mixtures | 26 |
| 3.14 | Diffusion coefficients for Ar/CO2 93/7, Ar/CO2+0.79N2, Ar/CO2+0.21O2 mixtures | 26 |
| 3.15 | Mesh transparency for pure argon and Ar/CO2 93:7 compared with the case of air additions | 27 |
| 3.16 | Distribution of the number of electrons produced by an electron in pure argon and Ar/CO2 93/7 compared with the case of air additions. | 27 |
| 3.17 | Transparency study for different air additions in the gas mixture Ar/CO2 (finer meshing size). | 28 |
| 4.1 | Geant4 classes diagram | 30 |
| 4.2 | Top: Volcanoes of the Hellenic arc. Arrows show the direction of plate movement. Left: Geological map of Methana. Right: Map of Methana. | 31 |
| 4.3 | Schematic view of the geometry. Left: Top view. Right: Side corner view. | 32 |

| | |
|--|----|
| 4.4 Muon track (red) of 4 GeV in rock. Green tracks refer to neutral particles. The muon experiences 275 ionizations and its range is about 8.07 m. | 32 |
| 4.5 Simulation result for muon energy loss in rock. Magenta line: Total energy loss, Blue line: Ionization component, Red line: Pair production component, Green line: Bremsstrahlung component | 33 |
| 4.6 Simulation result for muon range in rock. | 33 |
| 4.7 Schematic of the method used for the calculation of scattering angles | 34 |
| 4.8 Scattering effect for 1k muons with energies of 500 GeV. | 34 |
| 4.9 Scattering effect for 1k muons with energies of 600 GeV. | 35 |
| 4.10 Scattering effect for 1k muons with energies of 700 GeV. | 35 |
| 4.11 Scattering effect for 1k muons with energies of 800 GeV. | 36 |
| 4.12 Scattering effect for 1k muons with energies of 900 GeV. | 36 |
| 4.13 Distributions of scattering angles for different energies. Stacked histograms Fig. 4.8 - 4.12 | 37 |
| 4.14 Distribution of scattering angles as a function of muon's energy. | 37 |
| 4.16 Scattering effect. The detector volume is divided into 1x1 m pixels. Top Left: 1000 muons with initial energy of 900GeV. Top Right: 2000 muons with initial energy of 900GeV. Bottom: 5000 muons with initial energy of 900GeV. | 38 |
| 4.18 Scattering effect. The detector volume is divided into 0.5x0.5 m pixels. Top Left: 1000 muons with initial energy of 900GeV. Top Right: 2000 muons with initial energy of 900GeV. Bottom: 5000 muons with initial energy of 900GeV. | 39 |
| 4.21 Energy distribution, in detector, of muons of different initial energy after crossing the volcano | 40 |

Bibliography

- [1] B. Rossi, "Cosmic Rays", McGraw-Hill Book Company Inc, 1964
- [2] T. Gaisser, "Cosmic Rays and Particle Physics", Cambridge University Press, 1990
- [3] P. K.F. Grieder, "Cosmic Rays at Earth", Elsevier, 2001
- [4] H. M. Portella et al. , "Muon spectra at sea level"
- [5] S. Cecchini, M. Spurio, "Atmospheric muons: experimental aspects", Geoscientific Instrumentation Methods and Data Systems, 2012
- [6] C. Patrignati et al. (Particle Data Group), "Particle Physics Booklet", 2016
- [7] Keary P., Brooks M., Hill I., " An Introduction to Geophysical Exploration", 3rd Edition, Wiley-Blackwell, 2002
- [8] George E.P., "Cosmic rays measure overburden of tunnel", Commonwealth Engineer: 455, 1955
- [9] Alvarez L.W, "Search for hidden chambers in the pyramids using cosmic rays", Science vol. 167, 1970
- [10] Malmqvist et al., "Theoretical studies of in-situ rock density determination using cosmic-ray muon intensity measurements with application in mining geophysics", Geophysics, 1979
- [11] Nagamine et al., "Geo-tomographic observation of inner-structure of volcano with cosmic-ray muons", Journal of Geography, 1955
- [12] Hiroyuki K.M Tanaka et al., "High resolution imaging in the inhomogeneous crust with cosmic-ray muon radiography: The density structure below the volcanic crater floor of Mt. Asama, Japan", Earth and Planetary Science Letters, 2007
- [13] Nishiyama R. et al., "Integrated processing of muon radiography and gravity anomaly data toward the realization of high-resolution 3-D density structural analysis of volcanoes: Case study of Showa-Shinzan lava dome, Usu, Japan", Journal of Geophysical Research, 2014
- [14] Hiroyuki K.M Tanaka et al., "Radiographic visualization of magma dynamics in an erupting volcano", Nature Communications5, 3381 (2014)
- [15] Buontempo S. et al., "Perspectives for the radiography of Mt. Vesuvius by cosmic ray muons", Earth, Planets and Space, vol 62, 2010
- [16] D. Carbone et al. , "An experiment of muon radiography at Mt Etna (Italy)", Geophysical Journal International, 2013
- [17] Tioukov V. et al., "Muography with nuclear emulsions - Stromboli and other projects", Annals of Geophysics, 2016
- [18] Lesparre N. et al., "Density muon radiography of La Soufriere of Guadeloupe volcano: comparison with geological, electrical resistivity and gravity data", Geophysical Journal International, vol 90, 2012
- [19] Noli P., et al., "Muography of the Puy de Dome", Annals of Geophysics, 2017
- [20] N. Kume et al., "Muon trackers for imaging a nuclear reactor", JINST 11 P09008, 2016
- [21] Blackwell T.B. et al., "Identification of nuclear materials in cargo containers using cosmic rays", IEEE, 978-1-4799-0534-8/13 2013
- [22] Heck D. et al., "CORSIKA: A Monte-Carlo code to simulate extensive air showers", Karlsruhe University, Forschungszentrum Karlsruhe, Report FZKA 6019, 1998
- [23] S. Bouteille et al. , "A Micromegas-based telescope for muon tomography: The WatTo experiment", Nuclear Instruments and Methods in Physics Research A, 2016
- [24] K. Nagamine et al., "Method of probing inner-structure of geophysical substance with the horizontal cosmic-ray muons and possible application to volcanic eruption prediction", Nucl. Instr. Meth., 1994

- [25] Athanassas C.D. et al., "Cosmic ray physics meets geology to monitor geohazards: Muon radiography of critical volcanoes in the Aegean", New Technologies, Hazards and Geoarcheology, 3 November 2017, Athens, Greece
- [26] L. G. Christophorou, "Electron-Molecule Interactions and their Applications", Volume I, Academic Press, Inc, 1984
- [27] T. Alexopoulos et al., "A spark-resistant bulk-Micromegas chamber for high rate applications", Nucl. Instrum. and Meth. A640 (2011) 110-118
- [28] G. A. Iakovidis, "Research and Development in Micromegas Detector for the ATLAS Upgrade", 2014
- [29] Y. Kataoka et al., "Performance studies of a micromegas chamber in the ATLAS environment", JINST 9 C03016, 2014
- [30] Bouteille S., "A Micromegas-based telescope for muon tomography: The WatTo experiment", Nucl. Instr. Meth., 2016
- [31] Lesparre N. et al., "Design and operation of a field telescope for cosmic ray geophysical tomography", Geosci. Instrum. Method Data Syst., 2012
- [32] F. Sauli, Principles of operation of multiwire proportional and drift chambers, Lectures 1975-1976, Geneva, pg. 33-34
- [33] H. Raether, "Electron Avalanches and Breakdown in Gases", Butterworths, 1964
- [34] Townsend J.S, "Electricity in Gases", Oxford University Press, Oxford, UK, 1915
- [35] Geant4 Collaboration Group, Geant4 User's Guide
Website: <http://geant4.web.cern.ch/geant4>
- [36] C. Geuzaine, J.F. Remacle, Gmsh Reference Manual
Website: <http://gmsh.info>
- [37] J. Ruokolainen, M. Malinen, P. Råback, T. Zwinger, A. Pursula, M. Byckling, ElmerSolver Manual, CSC - IT Center for Science.
Website: <https://www.csc.fi/web/elmer>
- [38] H. Schindler, Garfield++ User Guide.
Website: <http://garfieldpp.web.cern.ch/garfieldpp>
- [39] R. Brun, F. Rademakers, P. Canal, I. Antcheva, D. Buskulic, ROOT Users Guide
Website: <https://root.cern.ch>